Local Rapid Exhumation and Fast Cooling in a Long-lived Paleoproterozoic Orogeny

Yi Zou[1,2,3]*, Xu Chu [iD] [2], Qiuli Li[1,3], Ross N. Mitchell[1], Mingguo Zhai[1,4], Xinyu Zou[3], Lei Zhao[1], Yuquan Wang[1,3] & Bo Liu[1,3]

[1]State Key Laboratory of Lithospheric Evolution, Institute of Geology and Geophysics, Chinese Academy of Sciences, Beijing, China; [2]Department of Earth Sciences, University of Toronto, Toronto, ON M5S 3B1, Canada; [3]Innovation Academy for Earth Sciences, Chinese Academy of Sciences, Beijing, China; [4]Key Laboratory of Computational Geodynamics, University of Chinese Academy of Sciences, Beijing, China

*Corresponding author. Telephone: +86-01082998255. E-mail: zouyijiangxi@126.com

ABSTRACT

The exhumation and cooling rates of high-grade metamorphic rocks are crucial for inferring orogenic processes and understanding the regimes of heat transport in the Earth's crust. Quantification of these rates remains challenging for Precambrian terranes, because the temporal resolution of geochronology becomes coarser in deeper geological time. This limitation is partly reflected by a striking lack of Proterozoic or older short-duration events ($<$10 Myr); most documented cases of fast metamorphism are confined to the Phanerozoic. In this study, we use garnet geospeedometry to explore the metamorphic rates of Paleoproterozoic high-grade rocks from two representative areas within the long-lived (1·95–1·80 Ga) Jiao-Liao-Ji orogenic belt, North China Craton. The pelitic granulites in the Taipingzhuang area record high-pressure granulite-facies (HPG) metamorphism of $\sim$12 kbar and $\sim$800 °C, followed by a fast decompression-cooling to $\sim$5 kbar and $\sim$600 °C within $\sim$5 Myr, at *c.* 1·87 Ga. The pelitic granulites in the Rizhuang area document a brief ($<$1 Myr) thermal excursion to ultrahigh-temperature (UHT) metamorphism of $\sim$8 kbar and $\sim$940 °C at *c.* 1·85 Ga, followed by a fast cooling to $\sim$600 °C within 1–5 Myr. In light of available geological data, the fast decompression-cooling of HPG granulites is interpreted as the syn-collisional exhumation of thickened lower crustal segments at *c.* 1·87 Ga, most probably through tectonic extrusion. The thermal excursion transiently reaching UHT conditions is inferred to be triggered by localized syn-metamorphic mafic intrusions in association with magmatic underplating during post-collisional extension at *c.* 1·85 Ga. These metamorphic pulses were interspersed within the protracted Paleoproterozoic orogenesis and require geodynamic processes resembling modern plate tectonics. Notably, these ancient rapid events are beyond the temporal resolution of commonly used *in situ* geochronology, which tends to yield apparent longer durations given errors and uncertainties. We therefore note that most ancient metamorphic rates might be underestimated using geochronological data, and recommend garnet geospeedometry as a promising alternative approach. The largely similar rates recorded by Paleoproterozoic and Phanerozoic orogens, as well as high-pressure metamorphism at 1·9–1·8 Ga, support the operation of modern plate tectonics in Paleoproterozoic time.

Key words: Jiao-Liao-Ji orogen; fast metamorphism; garnet diffusion modeling; geochronology; plate tectonics

INTRODUCTION

Determining the timescales or rates of metamorphic imprints is critical for deciphering the kinematics of subduction, orogenesis, and other tectonic–metamorphic processes (England & Thompson, 1984; Thompson & England, 1984; Chu et al., 2017; Ibanez-Mejia et al., 2018; Viete et al., 2018). The exhumation and cooling rates of regional high-grade rocks are of particular importance to quantifying orogenic dynamics and the regimes of heat transport in the Earth's crust (Willigers et al., 2002; Reiners et al., 2003; Sorcar et al., 2014; Chu et al., 2018; Chowdhury & Chakraborty, 2019), and serve as benchmarks for thermo-mechanical numerical models aimed at understanding both present-day and ancient geodynamics (Gerya et al., 2008; Gapais et al., 2009; Jamieson & Beaumont, 2011; Gerya, 2014; Sizova et al., 2014). Accurate determination of such metamorphic rates therefore remains a longstanding goal of metamorphic petrology (e.g. Engi et al., 2017), but has been particularly challenging for rocks in ancient orogens.

Current radiometric geochronology has an inherent uncertainty (external error or reproducibility) so that its temporal resolution is inevitably coarser in deeper geological time (e.g. Schaltegger et al., 2015). For example, in situ zircon U–Pb dating methods, secondary ion mass spectrometry (SIMS) and laser ablation inductively coupled plasma mass spectrometry (LA-ICP-MS) have a conservative uncertainty of 1–4% (e.g. Li et al., 2015). Such an uncertainty means the temporal resolution exceeds 18 Myr when applied to rocks older than 1·80 Ga, and is thus unable to recognize ancient short-duration metamorphism (<10 Myr). This is partly reflected by the interesting fact that hitherto reported examples of short-duration metamorphism (<10 Myr; Viete & Lister, 2017) are nearly all confined to young orogenic belts mainly after the late Neoproterozoic (Rubatto & Hermann, 2001; Pauly et al., 2016; Viete & Lister, 2017), and are strikingly rare in the early Precambrian (Collins et al., 2004; Baldwin et al., 2007; Guevara et al., 2017; Viete & Lister, 2017). It remains uncertain whether the scarcity of Precambrian short-duration metamorphism is dominantly either an artifact of geochronological uncertainties or a real reflection of different tectonic regimes. The dichotomy of metamorphic rates has fueled debate about the extrapolation of modern plate tectonics back to the early Precambrian (Willigers et al., 2002; Gerya et al., 2008; Zhai et al., 2009; Chowdhury et al., 2017; Zhou et al., 2017; Chowdhury & Chakraborty, 2019).

Garnet chemical zoning in the four major components (almandine, spessartite, pyrope, and grossular) provides an extensive record of the thermal histories of metamorphic rocks (Caddick et al., 2010; Ganguly, 2010; Ague & Carlson, 2013; Chu & Ague, 2015). The diffusion coefficients of the four major divalent cations (Fe, Mn, Mg, and Ca) in natural garnet have been extensively calibrated by a variety of experimental and field-based studies (e.g. Carlson, 2006; Ganguly, 2010). These data yield several diffusion models that mathematically describe the diffusivities of the divalent cations (Chakraborty & Ganguly, 1992; Carlson, 2006; Borinski et al., 2012; Chu & Ague, 2015). These models agree with each other at granulite- to upper amphibolite-facies conditions, although downward extrapolations to <600 °C can lead to about one order of magnitude differences (Chu & Ague, 2015). Based on these models, diffusion simulations of garnet zoning (garnet geospeedometry) have placed important constraints on the timescales of metamorphic processes and pressure–temperature–time (P–T–t) evolution (Florence & Spear, 1995; Ganguly et al., 1998, 2000; Gaidies et al., 2008; Caddick et al., 2010; Ganguly, 2010; Ague & Carlson, 2013; Pauly et al., 2016; Chu et al., 2017; Guevara et al., 2017; Viete & Lister, 2017; Chu et al., 2018; Viete et al., 2018). This method applies to garnet that can be directly linked to metamorphic evolution, and hence can provide a consistent record of thermal history (Faryad & Chakraborty, 2005; Caddick et al., 2010; Chu et al., 2018). More importantly, garnet geospeedometry is capable of resolving timescales shorter than one thousand years, independent of rock ages, and therefore can be a promising means to constrain ancient metamorphic rates.

During the Paleoproterozoic era (2·1–1·8 Ga), a number of linear orogenic belts developed on a global scale, resulting in the assembly of the supercontinent Columbia/Nuna (Fig. 1a), possibly Earth's first true supercontinent (Hoffman, 1989; Zhao et al., 2002; Evans & Mitchell, 2011; Wan et al., 2015). These belts are distinct from typical Archean granite–greenstone belts but resemble Phanerozoic orogens in many ways. High-pressure granulite-facies (HPG), ultrahigh-temperature (UHT) and ultrahigh-pressure metamorphisms are recognized within these ancient belts (Fig. 1a; Zhai & Liu, 2001; Zhao et al., 2001, 2004; Santosh et al., 2006; Zhai et al., 2009; Ganne et al., 2012; Glassley et al., 2014; Weller & St-Onge, 2017; Zhou et al., 2017; Brown & Johnson, 2018; Xu et al., 2018a), spurring the speculation that modern plate tectonics may have been operative globally by this time (Xu et al., 2018a). Despite its geodynamic importance, the exhumation and cooling mechanisms of these rocks are not well understood, mainly owing to the limited knowledge of their timescales. Accurately quantified rates, in concert with P–T–t paths, can thus provide insights into Paleoproterozoic plate tectonics.

In this contribution, we focus on HPG and UHT pelitic granulites, from two representative areas within the Paleoproterozoic Jiao-Liao-Ji orogenic belt (Fig. 1b and c). Two previous studies estimated a slow time-integrated exhumation rate of 0·18–0·24 mm a^{-1} assuming uniform exhumation throughout the belt (Zhou et al., 2017; Zou et al., 2017). However, petrographic observations and garnet zoning of some pelitic granulites suggest that the exhumation and cooling may have
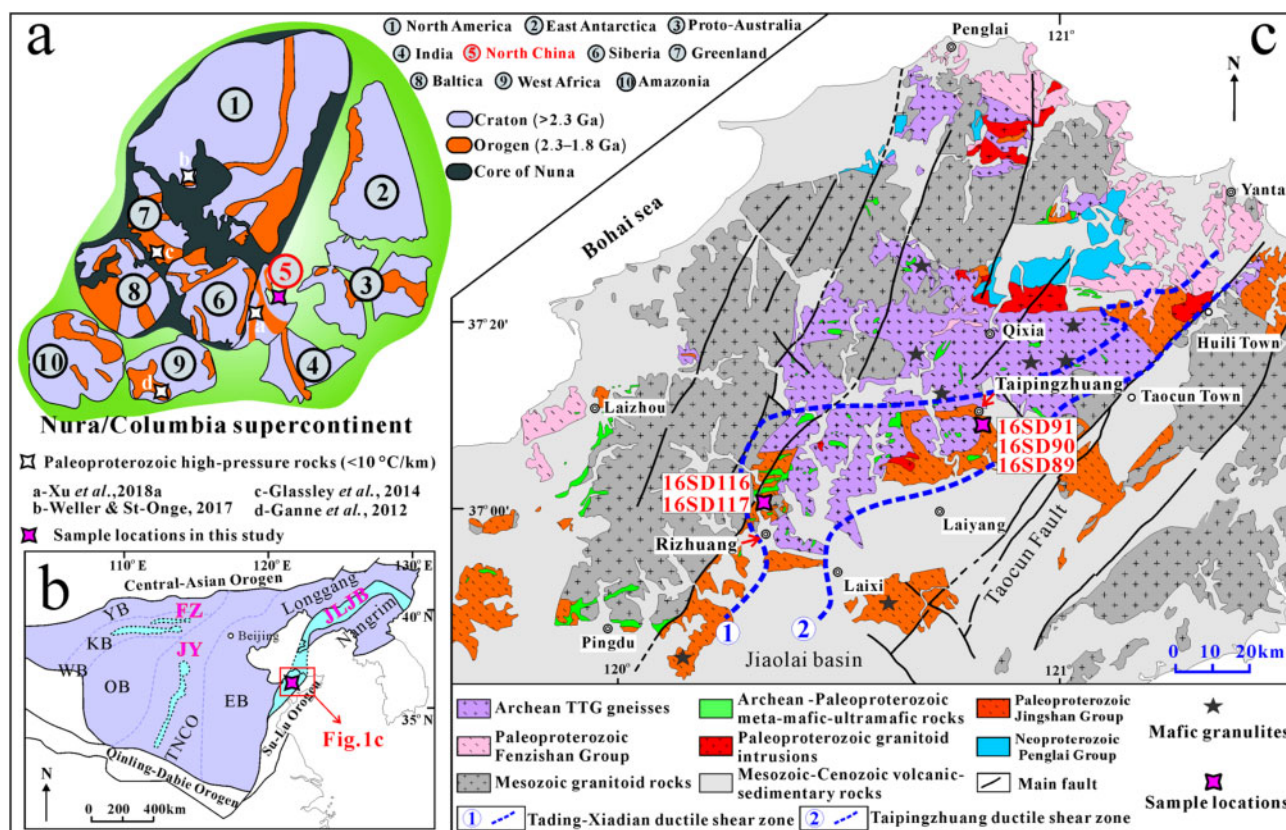
Fig. 1. (a) Reconstruction of the supercontinent Nuna/Columbia at 1·8–2·1 Ga and the location of the North China Craton (modified after Wan *et al.*, 2015; Zou *et al.*, 2020). White stars denote the locations of Paleoproterozoic high-pressure rocks with low thermal gradients (<10 °C km⁻¹) that mark cold subduction processes (data from Ganne *et al.*, 2012; Glassley *et al.*, 2014; Weller & St-Onge, 2017; Xu *et al.*, 2018a). Purple star represents the sample location in this study. (b) Tectonic division of the North China Craton and the location of the Jiaobei terrane (modified after Zhao & Zhai, 2013). EB, Eastern Block; FZ, Fenzhen belt; JLJB, Jiao-Liao-Ji belt; JY, Jinyu belt; KB, Khondalite belt; OB, Ordos Block; TNCO, Trans-North China Orogen; WB, Western Block; YB, Yinshan Block. (c) Regional geology of the Jiaobei terrane and sample localities (modified after Li *et al.*, 2012; Zou *et al.*, 2018).

taken place at a much faster rate. In this study, we explore these rates by garnet geospeedometry in concert with an integrated study of petrology, phase equilibria modeling, geothermobarometry, and multi-mineral U–Pb geochronology. The metamorphic rates obtained by diffusion modeling are compared with geochronological constraints and those retrieved from young collisional zones of modern plate tectonics. These comparative studies shed light on ancient metamorphic rates and the nature of the Paleoproterozoic tectonic regimes.

REGIONAL GEOLOGY

The Jiao-Liao-Ji orogenic belt (JLJB) represents one of the three Paleoproterozoic orogenic belts within the North China Craton (NCC) (Fig. 1b; Zhao & Zhai, 2013). The tectonic evolution of these Paleoproterozoic orogenic belts has been a topic of global attention regarding their role in the supercontinent assembly (Fig. 1a; Hoffman, 1989; Zhao *et al.*, 2002; Wan *et al.*, 2015), and tectonic regimes related to the global emergence of plate tectonics involving deep subduction (Xu *et al.*,

2018a), accretion, and collisional processes (Zhao & Zhai, 2013). The JLJB extends for ~1200 km between the Longgang and Nangrim blocks (Fig. 1b), and is dominated by metasedimentary and metavolcanic successions typical of khondalite-series rock associations (Lu *et al.*, 1996; Lu *et al.*, 2005; Li & Chen, 2014; Liu *et al.*, 2015a). These successions were deposited during a rifting event at 2·2–2·1 Ga (Xu *et al.*, 2018b), and were metamorphosed and deformed at 1·95–1·80 Ga (e.g. Liu *et al.*, 2015a; Xu & Liu, 2019). This is similar to the rifting event in the northern Superior Craton that preceded the Trans-Hudson Orogeny at *c.* 1·83 Ga (Weller & St-Onge, 2017). Recent studies have revealed a Paleoproterozoic granulite-facies metamorphic event with clockwise *P–T* paths within the JLJB (Zhou *et al.*, 2004; Tam *et al.*, 2012a, 2012b; Liu *et al.*, 2013c; Liu *et al.*, 2015c; Cai *et al.*, 2017; Zou *et al.*, 2017, 2019). These studies lead to a new tectonic model involving an initial phase of rifting, a subsequent opening of an ocean basin, and the final closure of the ocean basin through subduction and collision (e.g. Liu *et al.*, 2015a).

Our study area, the Jiaobei terrane (Fig. 1c), is located in the SW of the JLJB (Fig. 1b). It has an

Archean basement dominated by tonalitic–trondhjemitic–granodioritic (TTG) gneisses (Fig. 1c; Tang *et al.*, 2007; Zhou *et al.*, 2008a; Liu et al., 2011a, 2013a, 2015b). Unconformably overlying the basement, the Paleoproterozoic Jingshan and Fenzishan Groups constitute the lithological representative khondalite-series rocks of the JLJB (Fig. 1c), and are overlain by the Penglai (>1·80 Ga) and Zhifu Groups (Zhou *et al.*, 2008a; Liu *et al.*, 2013b). The Jingshan and Fenzishan Groups have similar protoliths, but display contrasting metamorphic grades. The Fenzishan Group is mainly greenschist to lower amphibolite facies whereas the Jingshan Group is mainly upper amphibolite to granulite facies (Fig. 1c; Zhou *et al.*, 2004; Li *et al.*, 2012; Tam *et al.*, 2012a, 2012b; Liu *et al.*, 2015c). The HPG pelitic granulites found in the Jingshan Group serve as the most important evidence of the collisional origin of the JLJB (Zhou *et al.*, 2004, 2008b; Tam *et al.*, 2012b; Zou *et al.*, 2017), coinciding with the collisional assembly of the NCC within the supercontinent Columbia (Fig. 1a; Zhao *et al.*, 2002, 2004; Rogers & Santosh, 2009; Zhao & Zhai, 2013). In addition, regional field mapping shows that some pelitic granulites in the Jingshan Group were locally intruded by mafic dykes in an extensional setting (Dong *et al.*, 2011; Liu *et al.*, 2015c). This field characteristic is similar to that identified in the contemporaneous Khondalite and Trans-North China belts where UHT metamorphism has been reported (Fig. 1b; Jiao & Guo, 2011; Jiao *et al.*, 2011; Guo *et al.*, 2012; Santosh *et al.*, 2012; Li & Wei, 2016; Yang & Wei, 2017).

SAMPLE DESCRIPTION

The samples studied were collected from two representative localities: (1) the Taipingzhuang area (three HPG pelitic granulites 16SD89, 16SD90, and 16SD91; Figs 1c and 2; Supplementary Data Fig. S1; all supplementary datasets are available at http://www.petrology.oxford journals.org), which is the locality for the first discovery of HPG pelitic granulites in the NCC (Zhou *et al.*, 2004); (2) the Rizhuang area near Laixi city, where we identify pelitic granulites reaching UHT metamorphism (two pelitic granulites 16SD116 and 16SD117; Figs 1c and 2; Supplementary Data Fig. S2).

Pelitic granulites in the Taipingzhuang area

The HPG pelitic granulites in the Taipingzhuang area directly overlie the Archean basement (Li *et al.*, 2012; Supplementary Data Fig. S1). These pelitic granulites show a prominent foliation defined by oriented kyanite/sillimanite, quartz, and biotite. Gray leucosome layers of quartz and feldspar parallel to the foliation (Fig. 2a, b and e) are interpreted as former melts derived from partial melting of the pelitic granulites (Liu *et al.*, 2014). Minor greenschist-facies pelitic units are exposed in the Taipingzhuang area.

The studied samples are mainly composed of garnet, quartz, sillimanite/kyanite, biotite, K-feldspar, and plagioclase (Fig. 3a), with minor muscovite, ilmenite, rutile, monazite, and zircon. Garnet consists of subhedral to euhedral porphyroblasts of 0·5–3 mm in size (Fig. 3a). These porphyroblasts show complex zones: (1) a diablastic core that encompasses multiphase inclusions of quartz + biotite + (rutile ± ilmenite) + muscovite without kyanite (Fig. 3c–e), where some inclusions display a weak inherent foliation (Fig. 3c); (2) a mantle zone with sparse inclusions of quartz, rutile, ilmenite, biotite, kyanite, and K-feldspar, with no muscovite (Fig. 3c and f); (3) an inclusion-free rim (Fig. 3a–c and h). Notably, among the examined garnets, the core-to-rim disappearance of muscovite and appearance of K-feldspar and kyanite inclusions are gradual. Multi-phase inclusions of rutile + muscovite + kyanite are also recognized within some garnet grains. Well-preserved kyanite grains are porphyroblastic and of 0·5–2·0 mm size and show an equilibrium contact with K-feldspar (Fig. 3a, b and g). K-feldspar is commonly perthitic (Fig. 3g). Sillimanite exhibits two types: (1) fine-grained fibrous intergrowths associated with plagioclase + biotite + quartz (Fig. 3a–c and h); (2) coarse-grained prismatic (Fig. 3a–c), pseudomorphs after kyanite (Zhou *et al.*, 2008b; Zou *et al.*, 2017), with relict kyanite revealed by Raman spectroscopy (Zhou *et al.*, 2008b). Plagioclase has three textural settings: (1) minor matrix plagioclase; (2) thin lamellae within perthite; (3) inclusions within garnet. Notably, some matrix plagioclases are zoned, with a darker core (Na-rich) surrounded by a brighter rim (Ca-rich) in back-scattered electron (BSE) images (Fig. 3h). In some instances, a thin plagioclase corona encircles kyanite porphyroblasts (Fig. 3g). Biotite flakes (<500 μm) are scattered throughout the matrix (Fig. 3a). Locally, fine-grained biotite + plagioclase + sillimanite intergrowths surround kyanite or sillimanite porphyroblasts (Fig. 3b and c), associated with interstitial quartz ribbons (Fig. 3b and c), implying restite–melt back-reactions and final melt crystallization (Waters, 2001; Indares *et al.*, 2008; Kriegsman & Alvarez-Valero, 2010; White & Powell, 2010; Holness *et al.*, 2011; Zou *et al.*, 2017). Both rutile and ilmenite are present as inclusions within garnet, and rutile predominates (Fig. 3d–f). In the matrix, ilmenite predominates, and only minor relict rutile is preserved. In samples from the same locality, matrix rutile is better preserved and is rimmed by ilmenite (Zhou *et al.*, 2004; Zou *et al.*, 2017).

Based on these petrographic observations, we identify four metamorphic stages (M₁–M₄; Table 1). The M₁ assemblage preserved as garnet core inclusions consists of muscovite, rutile, ilmenite, plagioclase, biotite, and quartz. These inclusions show some adjustments of their boundaries towards a low-energy configuration (Fig. 3d and e), suggesting that they may be coeval with garnet core growth during prograde metamorphism (Vernon *et al.*, 2008; Zou *et al.*, 2017). The inferred M₁ assemblage is consistent with the previous study of Zhou *et al.* (2004).

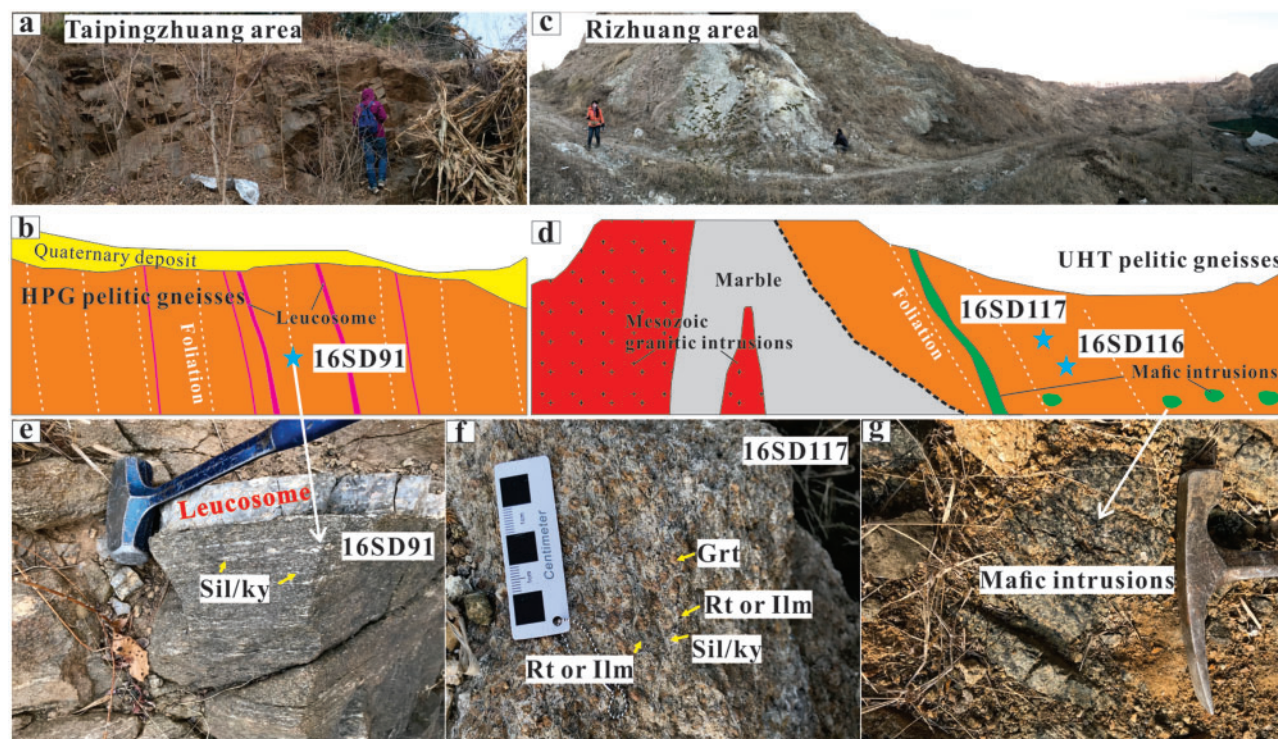The M₂ stage is represented by quartz, biotite, K-feldspar, plagioclase, kyanite and garnet porphyroblasts,

Fig. 2. Outcrop photographs of the representative pelitic granulites within the Jiaobei terrane. (a, b) Panoramic view and interpretation of the HPG pelitic granulites in the Taipingzhuang area. (c, d) UHT pelitic granulites and associated mafic intrusions in the Rizhuang quarry. The stars in (b) and (d) show sample locations. (e) Large kyanite/sillimanite grains in sample 16SD91. (f) Hand specimen of sample 16SD117, with large rutile grains. (g) Mafic intrusions.
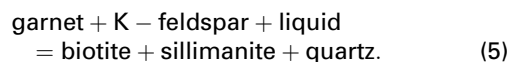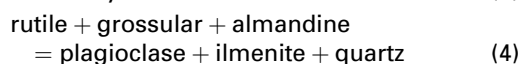
melt, and ilmenite. The presence of muscovite in the garnet core and its absence in the matrix suggest that the growth of kyanite and K-feldspar is prompted by the muscovite decomposition reaction (Spear *et al.*, 1999):

$$muscovite + quartz = K - feldspar + kyanite + melt. \quad (1)$$
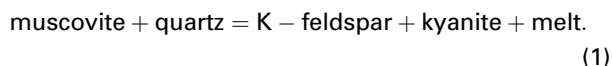
Additional reactants from biotite and kyanite inclusions are probably required to facilitate the growth of garnet through the following reaction (Spear *et al.*, 1999; O'Brien & Rotzler, 2003):

$$\begin{aligned} biotite + kyanite + quartz &= garnet + K - feldspar \\ &+ liquid. \quad (2) \end{aligned}$$
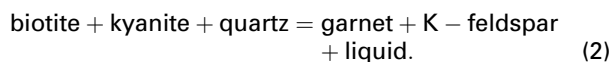
The M_3 stage is indicated by the transformation of kyanite to sillimanite, which is followed by the cooling stage (M_4) represented by the local intergrowths and final melt crystallization. The subdivision of these two stages is consistent with previous studies in this region (Zhou *et al.*, 2004, 2008b; Zou *et al.*, 2017). The following reactions are proposed for these stages (Bohlen & Liotta, 1986; Waters, 2001; Kriegsman & Alvarez-Valero, 2010):

$$kyanite = sillimanite \quad (3)$$

$$\begin{aligned} rutile + grossular + almandine \\ = plagioclase + ilmenite + quartz \quad (4) \end{aligned}$$

$$\begin{aligned} garnet + K - feldspar + liquid \\ = biotite + sillimanite + quartz. \quad (5) \end{aligned}$$

Pelitic granulites in the Rizhuang area

The pelitic granulites exposed in the Rizhuang area are closely associated with mafic dikes or boudins (Fig. 2c, d and g) emplaced at *c.* 1·85 Ga (Dong *et al.*, 2011; Liu *et al.*, 2015c; Supplementary Data Fig. S2). Gray leucosomes are scarce, and the abundance of mafic dikes appears to increase toward the bottom of the outcrop (Fig. 2c and d).

A striking petrographic feature of the pelitic granulites is coarse rutile grains (up to 0·5–1·0 mm; Fig. 4a) that are visible in hand-specimen (Fig. 2f). Some rutile grains are replaced by ilmenite at rims (Fig. 4e). Garnet forms subhedral to euhedral porphyroblasts of 0·5–2 mm size. Garnet core domains enclose abundant inclusions of quartz, biotite, rutile, and minor plagioclase and ilmenite (Fig. 4g), whereas the rim is largely free of inclusions (Fig. 4b and g). In some cases, garnet rim domains contain oriented needle-like rutile inclusions. Local intergrowths of sillimanite + biotite ± plagioclase ± quartz develop near garnet (Fig. 4b and d), implying localized melt–residue back-reactions. Coarse-grained tabular sillimanites are pseudomorphous after kyanite (Fig. 4b and e). Minor relict kyanite
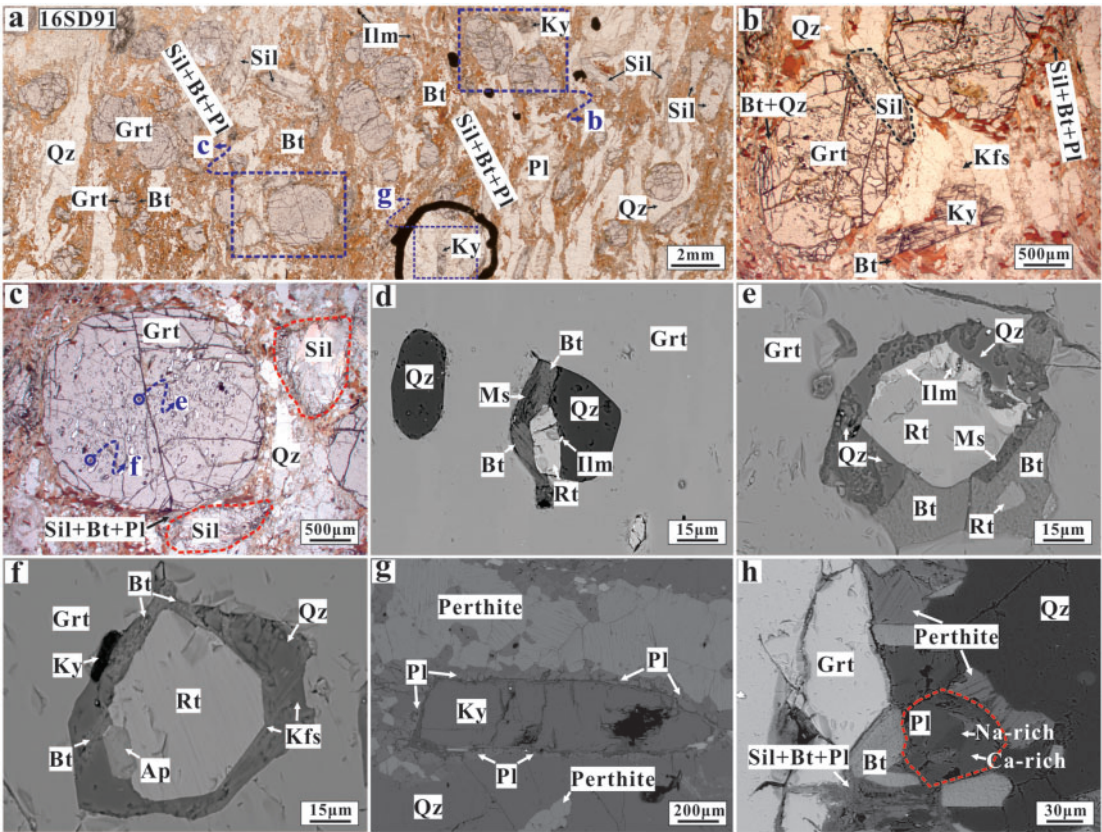
Fig. 3. Photomicrographs and back-scattered electron images of pelitic granulites from the Taipingzhuang area. (a) Part of thin section scanning image of the representative sample 16SD91 showing garnet and sillimanite/kyanite porphyroblasts in the matrix composed mainly of fine-grained biotite, sillimanite, plagioclase, K-feldspar, and interstitial quartz ribbon. Dashed blue rectangles denote the locations of the microdomains observed in (b), (c) and (g). (b) Well-preserved kyanite porphyroblast in contact with K-feldspar, and garnet rims locally eroded by biotite + quartz and biotite + sillimanite + plagioclase intergrowths. (c) The largest garnet grain observed in the thin section. Coarse-grained sillimanites are pseudomorphous after kyanite. The small blue circles represent the sites of observed inclusions shown in (e) and (f). (d, e) Rutile, muscovite, biotite, ilmenite, and quartz enclosed in the garnet core. (f) Polymineralic inclusions of rutile, kyanite, feldspar, biotite, and quartz in the garnet mantle domains. (g) K-feldspar is perthite and the kyanite porphyroblast is surrounded by a thin plagioclase corona. (h) Compositional zoned matrix plagioclase near garnet, with a Na-rich core surrounded by a Ca-rich rim. The fine-grained biotite + sillimanite + plagioclase intergrowths locally invade the garnet rim.

Table 1: Mineral assemblages and metamorphic stages of the pelitic granulites

Mineral	Sample 16SD91				Sample 16SD117			
	M_1	M_2	M_3	M_4	M_1 (not preserved)	M_2	M_3	M_4
Garnet	+	+	+	+		+	+	+
Quartz	+	+	+	+		+	+	+
Biotite	+	+	+	+		+		+
Sillimanite			+	+			+	+
Kyanite		+				+		
Plagioclase	+	+	+	+		+	+	+
K-feldspar		+	+			+	+	
Rutile	+					+		
Ilmenite	+	+	+	+		+	+	+
Muscovite	+							
Melt		+	+			+	+	

+, mineral is present in a mineral assemblage.

is found within these coarse-grained sillimanites or surrounded by the intergrowths (Fig. 4b and c). K-feldspar is perthitic and has a higher fraction of plagioclase lamellae (Fig. 4h) than the samples from the Taipingzhuang area. Matrix biotite is minor and is commonly present as local intergrowths, suggestive of a retrograde origin.

Based on the above observations, we suggest that the prograde M_1 assemblage in subsolidus conditions is not well preserved (Table 1). The presence of relict
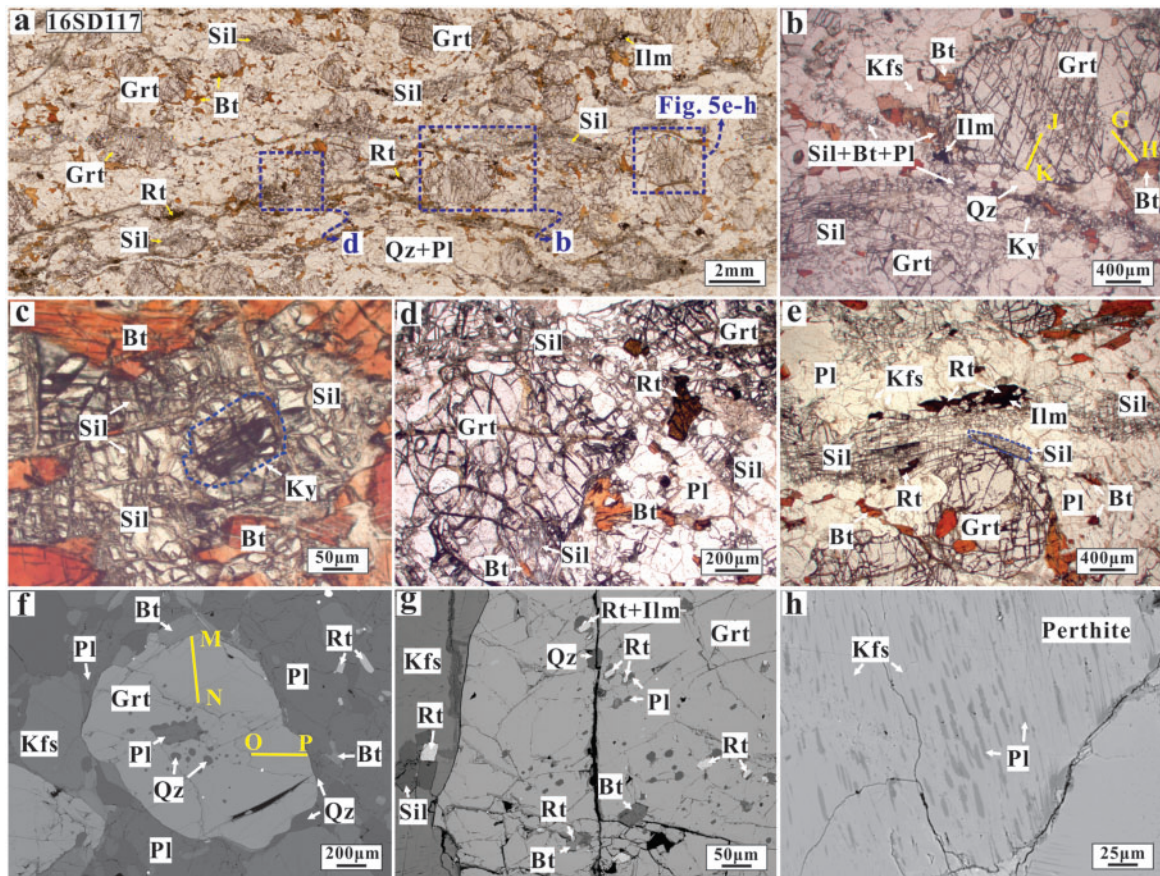
Fig. 4. Petrographic features of pelitic granulites from the Rizhuang area. (a) Portion of thin section scanning photograph displaying garnet porphyroblasts in matrix of sillimanite, feldspar, quartz, and rutile, with minor biotite. Dashed blue rectangles show the positions of the microdomains in (b) and (d), and the garnet chosen for X-ray mapping in Fig. 5e–h. (b) Coarse-grained sillimanite and garnet porphyroblasts. Local symplectites of fine-grained sillimanite + plagioclase + biotite + quartz grow inside the garnet rim and surround minor relict kyanite. Traverses G–H and J–K represent the compositional profiles shown in Fig. 7. (c) Minor relict kyanite within a coarse-grained sillimanite. (d) Well-preserved rutile grain in contact with coarse-grained sillimanite in the matrix, and garnet rim locally eroded by fibrous sillimanite + biotite symplectites. (e) Marginal replacement of rutile by ilmenite. The tabular sillimanite and minor biotite relics in the matrix should be noted. (f) Coarse-grained plagioclase inclusion within a garnet porphyroblast. It should be noted that the matrix quartz and plagioclase have cuspate boundaries, with low dihedral angles. Traverses M–N and O–P represent the analyzed profiles shown in Fig. 7. (g) Mineral inclusions of rutile, quartz, biotite, and minor plagioclase within garnet. (h) Perthite grain containing a relatively high proportion of plagioclase lamellae.

kyanite and rutile points to a high-pressure mineral assemblage (M_2) inferred to be garnet, quartz, K-feldspar, plagioclase, kyanite, rutile/ilmenite, biotite (inclusions), and melt. The wide occurrence of large matrix sillimanite and ilmenite grains rimming rutile grains implies that the M_2 assemblage is overprinted by a mineral assemblage (M_3) of sillimanite and ilmenite, probably accompanying garnet, quartz, K-feldspar, plagioclase, and melt. Matrix biotite is present only as local biotite + quartz $\pm$ sillimanite $\pm$ plagioclase retrograde intergrowths that denote the cooling stage (M_4).

MINERAL CHEMISTRY

We choose samples 16SD91 and 16SD117 as representative for detailed study. Analytical conditions for mineral chemistry and X-ray mapping of garnet (Fig. 5) are provided in Supplementary Material A1. Representative mineral and bulk-rock compositions are listed in Tables 2–5 and Supplementary Data Table T1 (rutile). Mineral abbreviations follow Whitney & Evans (2010) throughout the text.

Garnet

For sample 16SD91, we conducted X-ray mapping on the largest garnet observed in the thin section (Figs 3c and 5a–d) and measured two core-to-rim profiles on this garnet (Figs 5a and 6). The garnet is euhedral and has a pronounced bell-shaped Mn zoning pattern (Figs 5b and 6g, h). The Grs content in the diablastic core is about 0·11 (Fig. 6i), and decreases to 0·08–0·09 in the mantle (Fig. 6i and j) and to 0·06–0·04 in the rim (Fig. 6i and j). The X_{Mg} value is broadly stable at 0·27–0·29 throughout the core–mantle domains and decreases gradually to 0·20–0·22 in the rim, with an abrupt downturn to 0·16–0·18 at the grain boundary
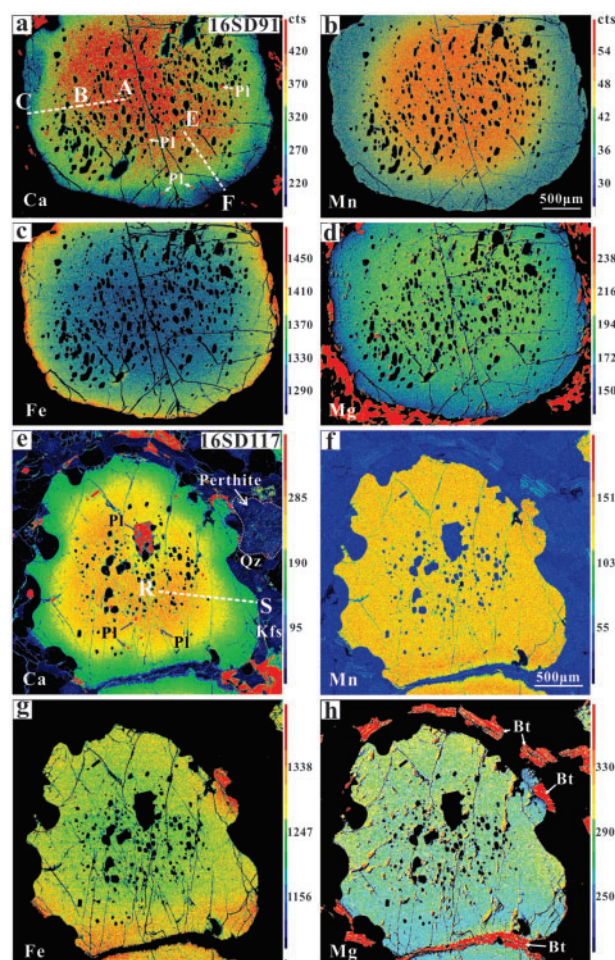
Fig. 5. X-ray mapping of the garnets shown in Figs 3c and 4a. Traverses A–B–C, E–F, and R–S denote the compositional profiles shown in Figs 6 and 7. It should be noted that there are some features of Ca-uptake in the garnet domains around plagioclase inclusions shown in (e).

(Fig. 6e and f). Smaller garnet grains have Sps, Grs, and X_{Mg} values similar to the mantle–rim domains of the largest garnet, suggesting that they were cut off-center.

In sample 16SD117, garnet core domains display some variations in Grs (0·05–0·07) and X_{Mg} values (0·36–0·38), especially near garnet fractures and plagioclase inclusions (Fig. 5e–g). A noticeable compositional zonation is observed in the domains within ∼300 μm of the edges (Fig. 5e–h), where Grs content decreases from the core domains to 0·03–0·04 in the rim (Fig. 7u–y). The X_{Mg} value of rim domains varies distinctly with textural relationships. Where a garnet rim is in contact with biotite, its X_{Mg} shows a rimward decreasing trend (Fig. 7k and m). In contrast, in garnet traverses toward a quartz or K-feldspar grain in the matrix, the X_{Mg} value increases toward grain edges (Fig. 7n and o), and the highest value is 0·39–0·41, similar to those reported from UHT pelitic granulites (e.g. Li & Wei, 2016).

Feldspar

In sample 16SD91, the plagioclase inclusions in garnet cores (Fig. 5a) are the most sodic (An = 0·11–0·12), and those enclosed in garnet mantle domains are more calcic (An = 0·13–0·22; Fig. 5a). Coarse-grained matrix plagioclases are zoned (Fig. 3h), with An contents of 0·17–0·21 in the core and 0·22–0·25 in the rim. Fine-grained plagioclase intergrowths and corona have similar An contents (0·23–0·27). Minor plagioclase lamellae in perthite are too thin to be accurately analyzed.

In sample 16SD117, coarse-grained euhedral plagioclase inclusions that are isolated within garnet or associated with quartz are the most Ca-rich (An = 0·50–0·51; Fig. 4f). Tiny subhedral plagioclases of the polymineralic inclusions of biotite + rutile + plagioclase in garnet (Fig. 4g) have lower An contents of 0·25–0·28. Matrix plagioclases have a narrow An range (0·37–0·39). The plagioclase lamellae within perthite (Figs 4h and 5e) have a wide An range of 0·05–0·37 (average of ∼0·27).

Muscovite and biotite

In sample 16SD91, muscovite inclusions in garnet have Si contents of 3·20–3·22 p.f.u. (per formula unit based on 11 oxygen) and X_{Mg} of 0·69–0·73 (Table 5). Biotite inclusions in garnet have high X_{Mg} (0·65–0·67) and variable Ti contents of 0·13–0·21 p.f.u. Matrix biotite is characterized by low X_{Mg} values of ∼0·55 and Ti contents of 0·17–0·23 p.f.u. In sample 16SD117, the minor matrix biotite has lower X_{Mg} values and higher Ti contents than the inclusion-type, being 0·68–0·69 vs 0·72–0·75 and 0·29–0·36 vs 0·30–0·32 p.f.u., respectively.

Rutile

Matrix rutile shows higher Nb and Cr contents than its inclusion counterpart (Fig. 8a and b). The highest Cr and Nb contents were measured from grains rimmed by ilmenite or near biotite, consistent with a retrograde effect by ilmenite and biotite (Fig. 8a and b; Chen *et al.*, 2018). The Zr-in-rutile thermometry of Tomkins *et al.* (2007) is employed in this study, with pressures constrained by phase modeling results (12 kbar for sample 16SD91; 10 kbar for sample 16SD117). Given the presence of zircon, rutile, and quartz in garnet and in the matrix, the activity of SiO_2 and $ZrSiO_4$ is considered as unity. The calculated temperatures of rutile inclusions show a core–rim variation in garnet (Fig. 8c). Isolated rutile inclusions in garnet cores record lower temperatures of 680–760 and 700–820 °C for samples 16SD91 and 16SD117, respectively; whereas those enclosed within 200–600 μm of the preserved garnet edges document higher temperatures of 780–800 and 850–920 °C (Fig. 8c). Similar to the study of Pauly *et al.* (2016), these trends probably reflect the prograde growth of garnet. Given that retrograde metamorphism tends to lower the Zr content of rutile (Meinhold, 2010), the maximum Zr content measured probably reflects a minimum

Table 2: Bulk-rock compositions for phase modeling (mol%)

	H_2O	SiO_2	Al_2O_3	CaO	MgO	FeO	K_2O	Na_2O	TiO_2	O
Sample 16SD91										
Measured bulk-rock composition	3·53	67·03	11·01	1·24	4·31	7·49	2·56	1·91	0·55	0·38
Measured bulk-rock composition minus 7 mol% garnet cores	3·53	68·77	10·75	0·98	3·82	6·50	2·75	1·97	0·59	0·34
Step 1 melt-reintegrated composition	4·92	66·50	10·80	1·20	4·06	7·06	2·56	2·04	0·52	0·35
Step 2 melt-reintegrated composition	6·36	65·93	10·58	1·15	3·82	6·65	2·55	2·15	0·49	0·33
Sample 17SD117										
Measured bulk-rock composition	0·85	59·14	13·52	2·12	6·21	11·36	3·18	2·25	1·13	0·24
Measured bulk-rock composition minus 5 mol% garnet cores	0·85	60·01	13·43	2·13	5·75	10·70	3·35	2·37	1·19	0·23

O is Fe_2O_3 measured by chemical titration, and FeO is total Fe. The H_2O content is determined by T–H_2O phase diagrams shown in Supplementary Fig. S3. The melt-reintegration method follows Korhonen *et al.* (2013). (See text for details.)

estimate of peak temperatures. This retrograde effect may be notable in sample 16SD117 as evidenced by a wider range of Zr contents and higher Cr contents of rutile inclusions (Fig. 8b).

PHASE EQUILIBRIA AND METAMORPHIC *P–T* EVOLUTIONS

Metamorphic *P–T* paths were constructed by phase equilibria (pseudosection) in the model chemical system of Na_2O–CaO–K_2O–FeO–MgO–Al_2O_3–SiO_2–H_2O–TiO_2–Fe_2O_3 (NCKFMASHTO) using the THERMOCALC software (version 3.33; Powell & Holland, 1988; updated in October 2009) and the internally consistent thermodynamic dataset ds55 (Holland & Powell, 1998; created in November 2003). The following solution models were used: garnet, silicate melt (liq), and biotite (White *et al.*, 2007, 2014); muscovite and paragonite (Coggon & Holland, 2002); cordierite (Holland *et al.*, 1998); ilmenite and hematite (White *et al.*, 2000, 2014); plagioclase and K-feldspar (Holland & Powell, 2003); spinel and magnetite (White *et al.*, 2002). Aluminosilicates, quartz, rutile, and H_2O are regarded as pure phases.

Our phase equilibria rely on determination of the reactive bulk composition of an equilibrium volume (see the review by Lanari & Duesterhoeft, 2019). In this study, the measured bulk-rock compositions by XRF-1500 X-ray fluorescence spectrometry (Supplementary Material A2) were used as reactive bulk compositions, and were normalized in the NCKFMASHTO system (Table 2). The $Fe^{2+}/(Fe^{2+} + Fe^{3+})$ ratio was determined by chemical titration. The H_2O content was initially estimated to be 2–4 and 0–2 mol% for samples 16SD91 and 16SD117, respectively, using the observed biotite volume percentages and the Ti–H substitution scheme of White *et al.* (2007). These H_2O contents were further evaluated in T–M_{H_2O} phase diagrams calculated at different pressures (Supplementary Data Fig. S3), and were fine-tuned to 3·53 and 0·85 mol% so that the observed peak mineral assemblage is modeled to be stable close to the solidus (e.g. Korhonen *et al.*, 2013; Wei, 2016). The CaO content associated with apatite was removed stoichiometrically on the basis of P_2O_5 contents. The preservation of granulite-facies assemblages as well as leucosomes observed in the field suggests that the metapelites underwent partial melting and melt loss during prograde to near-peak conditions (White *et al.*, 2004; Guevara & Caddick, 2016; Wei, 2016). Accordingly, the measured bulk-rock compositions represent melt-depleted residua and are only useful to evaluate peak to subsequent retrograde *P–T* evolution (Indares *et al.*, 2008; Korhonen *et al.*, 2013).

Chemical fractionation owing to garnet porphyroblast growth could affect modeled mineral assemblages and compositional isopleths [see the reviews by Lanari & Engi (2017) and Lanari & Duesterhoeft (2019)]. To evaluate this effect, we calculated two phase diagrams using bulk-rock compositions with garnet cores removed. Based on the petrographic scanning photograph and X-ray maps (Figs 3–5), garnet cores account for about 7 and 5 vol% of the total rock volume, for samples 16SD91 and 16SD117, respectively. Hence, 7 and 5 mol% garnets of averaged garnet core compositions were subtracted (Table 2). The water content and $Fe^{2+}/(Fe^{2+} + Fe^{3+})$ ratio were adjusted to be the same with the measured bulk-rock compositions (Table 2). These two phase diagrams are shown in Supplementary Data Figs S5 and S7.

Sample 16SD91 preserves a subsolidus prograde assemblage of muscovite + rutile + ilmenite + plagioclase + biotite + quartz (Table 1). We used the stepwise melt-reintegration method of Korhonen *et al.* (2013) to depict the prograde evolution. The start point to add melt was set at peak *P–T* conditions (∼12 kbar, ∼800 °C; Fig. 9b), and 6 mol% melt with an equilibrium composition at this point was reintegrated into the measured bulk-rock composition (Table 2). A second point to add 6 mol% melt was at 10 kbar, 750 °C, where the predicted amount of melt of the above melt-reintegrated rock composition is ∼1 mol%, and approximates the amount of melt remained on grain boundaries (Korhonen *et al.*, 2013). After the two steps of melt-reintegration, the resulting synthetic bulk composition has a water-saturated solidus at ∼650 °C, and the observed subsolidus mineral assemblage is predicted (Fig. 9c). This melt-reintegrated composition may differ from that of the true protolith. Nonetheless, the review by Bartoli (2017) concluded that reintegrating a certain amount of melt could reproduce a similar prograde history, despite the various melt-reintegration methods adopted.

Table 3: Representative compositions of garnet in samples 16SD91 and 16SD117

Sample:	The largest garnet in sample 16SD91										Inclusion-free garnet	
Texture:	core					mantle		inner rim		outer rim	core	rim
SiO$_2$	38·10	38·13	38·30	38·14	38·43	38·16	38·27	37·99	37·87	37·77	38·27	37·55
TiO$_2$	0·01	0·05	0·00	0·01	0·00	0·02	0·05	0·00	0·04	0·04	0·56	0·01
Al$_2$O$_3$	21·31	21·84	21·62	21·03	21·70	21·62	21·79	21·92	21·62	22·01	21·39	21·86
Cr$_2$O$_3$	0·09	0·02	0·04	0·01	0·02	0·05	0·02	0·01	0·04	0·04	0·02	0·02
FeO^T	28·36	28·26	28·86	29·16	30·06	30·44	30·50	32·91	33·18	35·25	30·56	34·72
MnO	1·15	1·11	1·14	1·16	1·10	1·06	0·96	0·68	0·64	0·64	0·79	0·60
MgO	6·34	6·33	6·20	5·95	6·15	6·17	6·02	5·15	5·00	4·02	6·26	3·95
CaO	3·99	4·11	4·15	4·24	3·13	3·10	2·94	2·15	1·82	1·44	3·05	1·38
Total	99·34	99·84	100·30	99·70	100·59	100·62	100·55	100·80	100·21	101·21	100·89	100·09
O	12	12	12	12	12	12	12	12	12	12	12	12
Si	2·997	2·981	2·987	3·000	2·996	2·976	2·988	2·982	2·996	2·982	2·980	2·996
Ti	0·000	0·003	0·000	0·000	0·000	0·001	0·003	0·000	0·002	0·002	0·033	0·001
Al	1·975	2·012	1·987	1·949	1·994	1·987	2·005	2·028	2·016	2·048	1·963	2·056
Cr	0·006	0·001	0·002	0·001	0·001	0·003	0·001	0·001	0·003	0·002	0·001	0·001
Fe^{3+}	0·024	0·018	0·038	0·050	0·013	0·055	0·011	0·007	0·000	0·000	0·010	0·000
Fe^{2+}	1·842	1·829	1·844	1·868	1·947	1·930	1·981	2·154	2·195	2·328	1·980	2·317
Mn	0·076	0·073	0·075	0·077	0·072	0·070	0·063	0·045	0·043	0·043	0·052	0·041
Mg	0·743	0·737	0·721	0·697	0·715	0·718	0·701	0·603	0·590	0·473	0·727	0·470
Ca	0·336	0·344	0·347	0·357	0·261	0·259	0·246	0·181	0·154	0·121	0·254	0·118
Total	8·000	8·000	8·000	8·000	8·000	8·000	8·000	8·000	8·000	8·000	8·000	8·000
X_{Mg}	0·29	0·29	0·28	0·27	0·27	0·27	0·26	0·22	0·21	0·17	0·27	0·17
Alm	0·61	0·61	0·62	0·62	0·65	0·65	0·66	0·72	0·74	0·79	0·66	0·79
Sps	0·03	0·02	0·02	0·03	0·02	0·02	0·02	0·02	0·01	0·01	0·02	0·01
Prp	0·25	0·25	0·24	0·23	0·24	0·24	0·23	0·20	0·20	0·16	0·24	0·16
Grs	0·11	0·11	0·11	0·12	0·09	0·08	0·08	0·06	0·05	0·04	0·08	0·04

Sample:	16SD117									
Texture:	core				mantle		outer rim near quartz		outer rim near biotite	
SiO$_2$	38·74	38·93	38·96	38·96	38·83	38·33	39·37	38·78	38·40	38·57
TiO$_2$	0·02	0·10	0·12	0·09	0·11	0·10	0·09	0·31	0·13	0·13
Al$_2$O$_3$	21·37	22·90	22·87	22·94	22·88	22·67	23·40	22·02	22·67	22·61
Cr$_2$O$_3$	0·01	0·00	0·01	0·00	0·00	0·00	0·00	0·04	0·01	0·03
FeO^T	28·59	26·90	27·04	27·03	26·97	27·05	26·96	27·01	30·30	29·48
MnO	0·37	0·39	0·41	0·38	0·41	0·39	0·41	0·46	0·42	0·42
MgO	9·00	9·36	9·40	9·24	9·30	9·32	9·78	10·33	7·32	7·97
CaO	2·36	2·01	1·99	2·00	1·96	1·74	1·16	1·28	1·18	1·28
Total	100·46	100·61	100·78	100·64	100·45	99·60	101·16	100·24	100·43	100·50
O	12	12	12	12	12	12	12	12	12	12
Si	2·977	2·968	2·965	2·970	2·965	2·953	2·978	2·962	2·978	2·977
Ti	0·001	0·006	0·007	0·005	0·006	0·006	0·005	0·018	0·008	0·008
Al	1·935	2·058	2·051	2·061	2·059	2·058	2·087	1·982	2·072	2·057
Cr	0·001	0·000	0·000	0·000	0·000	0·000	0·000	0·002	0·001	0·002
Fe^{3+}	0·108	0·000	0·003	0·000	0·000	0·018	0·000	0·056	0·000	0·000
Fe^{2+}	1·729	1·715	1·718	1·723	1·722	1·724	1·706	1·669	1·965	1·903
Mn	0·024	0·025	0·027	0·025	0·027	0·025	0·026	0·030	0·028	0·028
Mg	1·031	1·064	1·067	1·050	1·059	1·070	1·103	1·176	0·846	0·917
Ca	0·194	0·164	0·162	0·163	0·160	0·144	0·094	0·105	0·098	0·106
Total	8·000	8·000	7·999	7·998	7·999	7·998	7·998	8·000	8·000	7·999
X_{Mg}	0·36	0·38	0·38	0·38	0·38	0·38	0·39	0·41	0·30	0·33
Alm	0·58	0·58	0·58	0·58	0·58	0·58	0·58	0·56	0·67	0·64
Sps	0·01	0·01	0·01	0·01	0·01	0·01	0·01	0·01	0·01	0·01
Prp	0·35	0·36	0·36	0·36	0·36	0·36	0·38	0·40	0·29	0·31
Grs	0·06	0·06	0·06	0·06	0·05	0·05	0·03	0·03	0·03	0·04

FeO^T is total FeO and Fe^{3+} is determined by stoichiometric calculation of Droop (1987). Alm, almandine; Sps, spessartine; Prp, pyrope; Grs, grossular. $X_{Mg} = Mg/(Mg + Fe^{2+})$.

Sample 16SD91

The phase diagram computed using the measured bulk-rock composition of sample 16SD91 is shown in Fig. 9a and b and Supplementary Data Fig. S4. The peak M$_2$ assemblage of garnet + kyanite + K-feldspar + biotite + plagioclase + quartz + ilmenite + melt is well predicted in the phase diagram (Fig. 9a). The garnet zoning (Figs 5 and 6) shows that the X_{Mg} value is broadly stable at the mantle domains that enclose mineral inclusions of kyanite and K-feldspar (Fig. 3f), and decreases gradually to the rim that is characterized by elevated Alm and declined Prp contents. This pattern suggests that the garnet mantle domains document the peak conditions and the rim reflects diffusional modification during retrograde metamorphism. The isopleths of Grs (0·08 ± 0·01) and X_{Mg} (0·27 ± 0·01) from the mantle

Table 4: Representative compositions of plagioclase in samples 16SD91 and 16SD117

Sample:	16SD91										
Texture:	Inclusion in garnet core		Inclusion in garnet mantle			Plmc		Plmr		corona	intergrowth
SiO_2	64·21	64·28	63·77	63·14	62·71	63·49	62·23	62·41	61·90	61·27	60·94
TiO_2	0·00	0·04	0·00	0·00	0·02	0·00	0·00	0·02	0·02	0·04	0·01
Al_2O_3	21·35	21·12	21·93	22·53	22·97	22·33	22·75	23·27	23·37	23·67	23·12
FeO^T	0·17	0·16	0·05	0·08	0·11	0·13	0·33	0·14	0·35	0·46	1·04
MnO	0·00	0·03	0·00	0·02	0·02	0·02	0·01	0·01	0·01	0·02	0·03
MgO	0·04	0·01	0·00	0·00	0·00	0·02	0·02	0·01	0·02	0·02	0·08
CaO	2·50	2·41	2·87	3·69	4·56	3·52	4·32	4·65	4·88	5·53	4·75
Na_2O	10·24	10·74	10·06	9·06	8·92	9·31	8·80	8·93	8·12	7·99	8·61
K_2O	0·14	0·17	0·33	0·27	0·18	0·16	0·12	0·22	0·16	0·29	0·18
Total	98·66	98·96	99·01	98·80	99·49	98·97	98·59	99·66	98·83	99·29	98·74
O	8	8	8	8	8	8	8	8	8	8	8
Si	2·869	2·869	2·844	2·820	2·789	2·829	2·793	2·775	2·771	2·742	2·749
Ti	0·000	0·001	0·000	0·000	0·001	0·000	0·000	0·001	0·001	0·001	0·000
Al	1·124	1·111	1·153	1·186	1·204	1·173	1·203	1·219	1·233	1·249	1·229
Fe	0·007	0·006	0·002	0·003	0·004	0·005	0·012	0·005	0·013	0·017	0·039
Mn	0·000	0·001	0·000	0·001	0·001	0·001	0·000	0·000	0·000	0·001	0·001
Mg	0·003	0·000	0·000	0·000	0·000	0·001	0·001	0·001	0·001	0·001	0·005
Ca	0·120	0·115	0·137	0·177	0·217	0·168	0·208	0·222	0·234	0·265	0·230
Na	0·887	0·929	0·870	0·785	0·769	0·804	0·766	0·770	0·705	0·693	0·753
K	0·008	0·010	0·019	0·016	0·010	0·009	0·007	0·012	0·009	0·017	0·010
Total	5·017	5·043	5·024	4·987	4·996	4·991	4·991	5·006	4·969	4·987	5·016
An	0·12	0·11	0·13	0·18	0·22	0·17	0·21	0·22	0·25	0·27	0·23
Ab	0·87	0·88	0·85	0·80	0·77	0·82	0·78	0·77	0·74	0·71	0·76
Or	0·01	0·01	0·02	0·02	0·01	0·01	0·01	0·01	0·01	0·02	0·01

Sample:	16SD117										
Texture:	Large inclusion in garnet		Tiny inclusion in garnet			Plmc		Plmr		intergrowth	Pl_0
SiO_2	55·23	54·99	60·08	60·93	60·54	58·50	58·52	58·13	57·55	59·38	60·29
TiO_2	0·00	0·00	0·00	0·02	0·01	0·00	0·01	0·00	0·05	0·02	0·02
Al_2O_3	28·86	28·92	24·38	24·17	24·20	26·50	25·80	26·67	26·16	25·58	23·85
FeO^T	0·16	0·13	0·01	0·01	0·14	0·00	0·06	0·08	0·10	0·05	0·00
MnO	0·00	0·00	0·02	0·00	0·01	0·00	0·04	0·00	0·00	0·00	0·00
MgO	0·00	0·00	0·00	0·00	0·01	0·03	0·00	0·01	0·02	0·00	0·00
CaO	10·43	10·52	5·81	5·43	5·60	7·74	7·92	7·79	8·30	7·88	5·85
Na_2O	5·18	5·51	8·35	8·87	8·66	7·25	6·97	7·22	7·10	6·88	8·40
K_2O	0·47	0·31	0·07	0·25	0·14	0·16	0·11	0·15	0·14	0·12	0·21
Total	100·33	100·38	98·71	99·67	99·31	100·17	99·43	100·05	99·40	99·91	98·64
O	8	8	8	8	8	8	8	8	8	8	8
Si	2·481	2·471	2·705	2·720	2·713	2·610	2·629	2·599	2·595	2·650	2·720
Ti	0·000	0·000	0·000	0·001	0·000	0·000	0·000	0·000	0·002	0·001	0·001
Al	1·528	1·532	1·294	1·271	1·278	1·393	1·366	1·405	1·390	1·345	1·268
Fe	0·006	0·005	0·000	0·000	0·005	0·000	0·002	0·003	0·004	0·002	0·000
Mn	0·000	0·000	0·001	0·000	0·000	0·000	0·002	0·000	0·000	0·000	0·000
Mg	0·000	0·000	0·000	0·000	0·001	0·002	0·000	0·001	0·001	0·000	0·000
Ca	0·502	0·506	0·280	0·260	0·269	0·370	0·381	0·373	0·401	0·377	0·283
Na	0·451	0·480	0·728	0·768	0·752	0·627	0·607	0·626	0·621	0·596	0·735
K	0·027	0·018	0·004	0·014	0·008	0·009	0·006	0·008	0·008	0·007	0·012
Total	4·994	5·012	5·013	5·034	5·028	5·011	4·994	5·016	5·021	4·977	5·019
An	0·51	0·50	0·28	0·25	0·26	0·37	0·38	0·37	0·39	0·38	0·27
Ab	0·46	0·48	0·72	0·74	0·73	0·62	0·61	0·62	0·60	0·61	0·71
Or	0·03	0·02	0·00	0·01	0·01	0·01	0·01	0·01	0·01	0·01	0·01

Plmc and Plmr denote core and rim of matrix-type plagioclase, respectively. Pl_0, plagioclase lamellae within perthite.

domains intersect at $800 \pm 5\,^{\circ}C$ and 12 ± 1 kbar within the modeled M_2 assemblage (Fig. 9a and b). Within these *P–T* conditions, predicted An contents are consistent with the measured values of 0·17–0·21 from matrix plagioclase cores (Fig. 9b). The peak temperatures defined are also consistent with the measured maximum Zr contents of rutile enclosed within the mantle domains (780–800 °C; Fig. 8c). We note that the modeled peak M_2 assemblage is close to, but 1 kbar below, the rutile-out boundary (Fig. 9a). This discrepancy might

reflect the relict rutile in the matrix and can be explained by the uncertainties of thermodynamic models (Palin et al., 2016; Lanari & Duesterhoeft, 2019; and references therein).

The M_3 assemblage is predicted in the modeled bt–grt–liq–sil–pl domain (Fig. 9a). Within this domain, there is a good agreement between the measured X_{Mg} (0·21 ± 0·01) and Grs (0·05 ± 0·01) values from garnet rims, defining *P–T* conditions at $780 \pm 5\,^{\circ}C$ and 8 ± 1 kbar close to the solidus (Fig. 9b). Garnet does
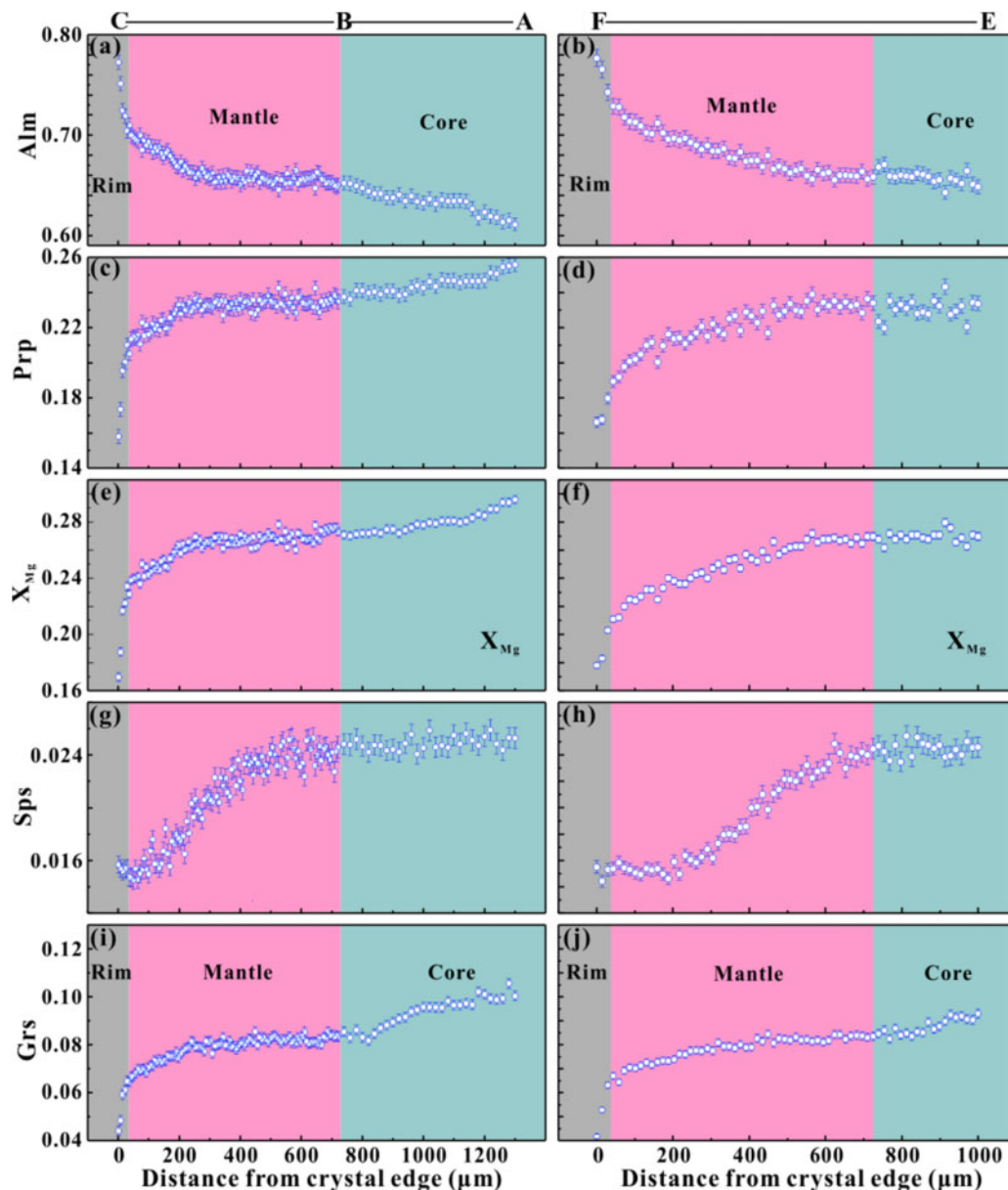
Fig. 6. Compositional profiles A–B–C and E–F shown in Fig. 5a.

not grow during the evolution from the M_2 to M_3 stages (Supplementary Data Fig. S4), so these *P–T* conditions represent a post-growth diffusional modification at garnet rims. The An isopleths (0·22–0·25) of plagioclase rims overlap the *P–T* conditions constrained by garnet (Fig. 9b). The late retrograde M_4 assemblage of fine-grained biotite + quartz ± sillimanite ± plagioclase intergrowths does not reach a global equilibrium and cannot be definitively mapped to the phase equilibria space. The GB thermometry (Holdaway, 2000) and GASP barometry (Holdaway, 2001) applied to garnet outermost rims and biotite and plagioclase in contact, as well as the Zr contents of matrix rutile (Fig. 8a and b), define the final *P–T* conditions of the M_4 stage at ∼5 kbar, ∼600 °C (Fig. 9b).

The phase diagram that considers garnet core fractionation shows almost identical phase relations (Supplementary Data Fig. S5). The modeled garnet X_{Mg} and Grs isopleths systematically shift to higher *P–T* domains by only ∼5 °C and 1–2 kbar that are indistinguishable within *P–T* uncertainties (Supplementary Data Fig. S5). The subsolidus prograde M_1 assemblage is predicted in the phase diagram after the two steps of melt-reintegration (Fig. 9c). The X_{Mg} values of garnet cores differ greatly from predicted ones owing to diffusional homogenization. However, the Grs contents of garnet cores and An values of the enclosed plagioclase inclusions are broadly consistent with predicted values in the subsolidus assemblage (Fig. 9c). The An and Grs contents could still preserve a trace of prograde information, owing to the sluggish diffusivity of Ca in garnet
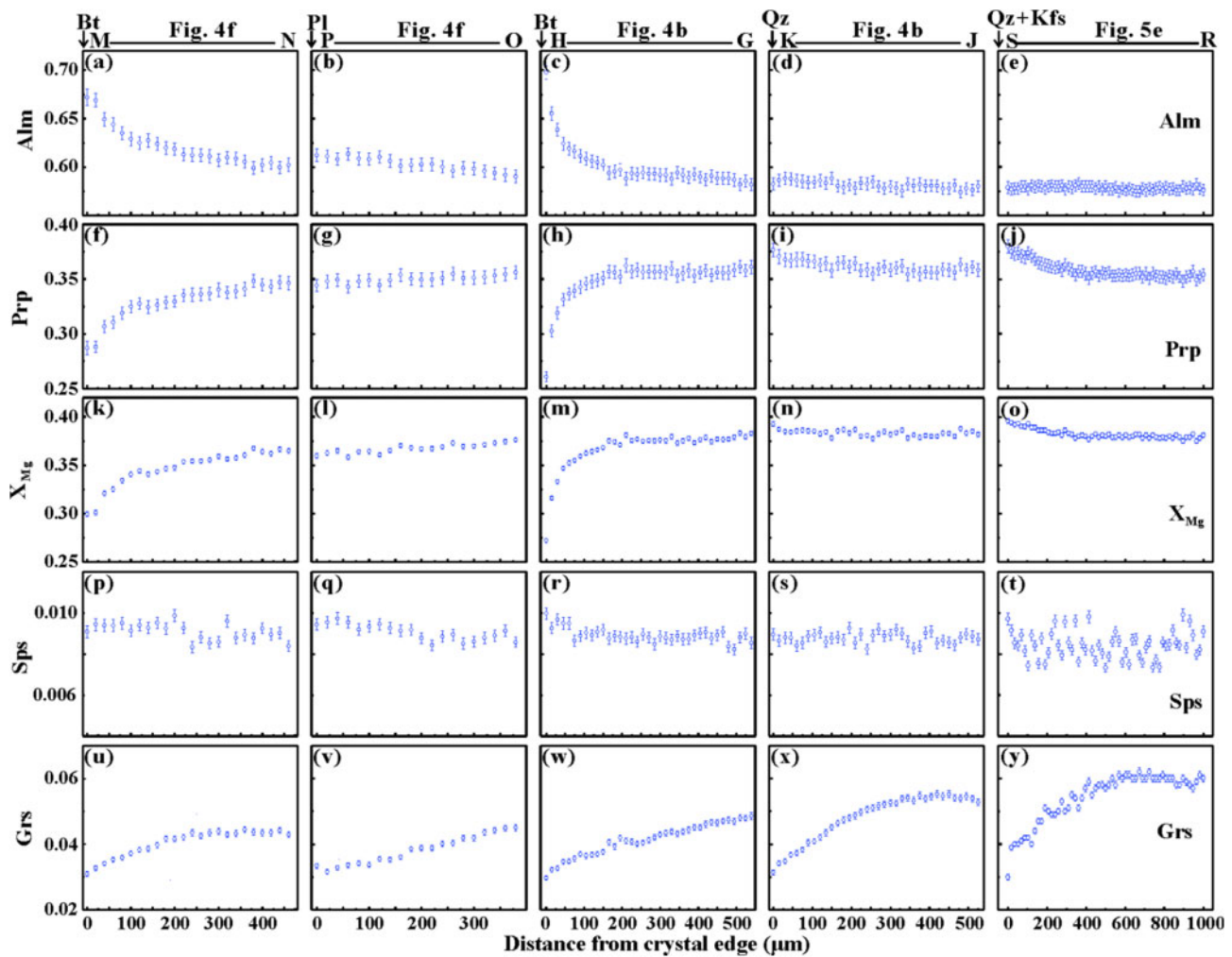
Fig. 7. Compositional profiles M–N, O–P, G–H, J–K, and R–S shown in Figs 4b, f and 5e.

(Chu & Ague, 2015) and plagioclase (Tajčmanová *et al.*, 2014). The prograde path from the M_1 to M_2 stages is characterized by a significant temperature increase. Along this path, the appearance of K-feldspar and kyanite and the decomposition of muscovite are consistent with the core-to-rim variation of inclusions in garnet (Fig. 3c–f) and the growth of kyanite and garnet porphyroblasts (Figs 3b and 9c).

Sample 16SD117

The *P–T* pseudosection calculated with the measured bulk-rock composition of sample 16SD117 is shown in Fig. 10 and Supplementary Data Fig. S6. The subsolidus prograde M_1 evolution that accounts for garnet core growth is not preserved, and hence melt-reintegration methods are not employed in this sample. The intersections of X_{Mg} (0.36 ± 0.01) and Grs contents (0.06 ± 0.01) from garnet core domains yield *P–T* conditions of 11 ± 0.5 kbar and 840 ± 5 °C, within the modeled M_2 assemblage of liq–bt–grt–pl–rt–ky (Fig. 10). Within these *P–T* conditions, the measured An contents (0.25–0.28)

from the tiny plagioclase inclusions within the garnet cores are broadly consistent with predicted ones (Fig. 10b; Supplementary Data Fig. S6). These *P–T* conditions are far above the garnet-in boundary, and thus probably reflect a re-equilibration at the M_2 stage. The X-ray mapping of the garnet cores shows a low-Ca moat around plagioclase inclusions (Fig. 5e), suggesting that Ca may have been extracted from the garnet cores surrounding the inclusions and incorporated into the plagioclases. Such a modification would result in lower Grs contents of garnet cores and higher An contents of plagioclase inclusions. In this case, the pressure conditions defined are possibly conservative, and the garnet core compositions represent a long re-equilibration at the M_2 stage.

The M_3 assemblage (liq–grt–pl–sil) reflects the transformation of kyanite to sillimanite and rutile to ilmenite (Fig. 10a). The temperature increase from the M_2 to M_3 stages is documented by the upturn of X_{Mg} profiles toward the garnet rims in contact with a quartz or K-feldspar grain (Fig. 7n and o). The intersections of the Grs contents and

Table 5: Representative compositions of biotite and muscovite in samples 16SD91 and 16SD117

Sample:	16SD91							16SD117			
Texture:	ms	ms	ms	Bt_{in}	Bt_{in}	Bt_m	Bt_m	Bt_{in}	Bt_{in}	Bt_m	Bt_m
SiO_2	48·90	49·97	50·12	37·85	39·14	36·74	36·55	36·61	36·57	35·74	35·53
TiO_2	0·20	0·46	0·78	2·43	3·87	3·07	4·14	5·78	5·45	5·66	6·54
Al_2O_3	33·69	34·24	34·56	19·43	18·30	17·55	18·50	15·43	15·71	17·44	16·42
Cr_2O_3	0·00	0·00	0·00	0·03	0·05	0·05	0·07	0·00	0·00	0·03	0·02
FeO^T	1·16	1·12	0·97	12·66	11·79	16·41	16·57	10·26	11·44	12·68	12·28
MnO	0·00	0·00	0·00	0·00	0·01	0·04	0·03	0·05	0·00	0·15	0·15
MgO	1·56	1·73	1·21	13·32	13·70	11·02	11·26	16·89	16·27	15·42	15·23
CaO	0·00	0·00	0·00	0·05	0·04	0·34	0·04	0·18	0·17	0·21	0·26
NiO	0·00	0·00	0·00	0·03	0·05	0·02	0·03	0·00	0·00	0·00	0·00
Na_2O	0·37	0·42	0·39	0·32	0·29	0·15	0·25	0·08	0·09	0·51	0·36
K_2O	9·89	10·00	8·90	9·33	9·04	9·42	9·26	9·98	9·35	9·04	8·72
Total	95·77	97·94	96·93	95·45	96·26	94·79	96·69	95·25	95·04	96·90	95·51
O	11	11	11	11	11	11	11	11	11	11	11
Si	3·209	3·204	3·221	2·766	2·815	2·770	2·699	2·692	2·697	2·614	2·619
Ti	0·010	0·022	0·038	0·134	0·210	0·174	0·230	0·320	0·302	0·288	0·363
Al	2·606	2·589	2·617	1·674	1·551	1·559	1·610	1·337	1·366	1·503	1·427
Cr	0·000	0·000	0·000	0·002	0·003	0·003	0·004	0·000	0·000	0·002	0·001
Fe	0·064	0·060	0·052	0·774	0·710	1·035	1·024	0·631	0·706	0·776	0·757
Mg	0·153	0·165	0·116	1·451	1·470	1·238	1·239	1·851	1·789	1·682	1·673
Mn	0·000	0·000	0·000	0·000	0·001	0·003	0·002	0·003	0·000	0·010	0·010
Ca	0·000	0·000	0·000	0·004	0·003	0·028	0·003	0·014	0·013	0·017	0·020
Ni	0·000	0·000	0·000	0·002	0·003	0·001	0·002	0·000	0·000	0·000	0·000
Na	0·047	0·052	0·049	0·045	0·040	0·022	0·036	0·012	0·013	0·073	0·052
K	0·828	0·818	0·730	0·870	0·830	0·906	0·872	0·936	0·880	0·843	0·820
Total	6·921	6·924	6·841	7·788	7·738	7·826	7·834	7·794	7·765	7·805	7·741
X_{Mg}	0·71	0·73	0·69	0·65	0·67	0·55	0·55	0·75	0·72	0·68	0·69

Bt_{in}, biotite inclusions within garnet; Bt_m, matrix-type biotite. $X_{Mg} = Mg/(Mg + Fe)$, assuming all the iron to be ferrous.s

the highest X_{Mg} values from the garnet rims suggest $P–T$ conditions of 8 ± 1 kbar, 920–1000 °C (Fig. 10b). The $P–T$ conditions are also consistent with the An contents of 0·37–0·39 from matrix plagioclases (Fig. 10b). The phase diagram calculated with the bulk-rock composition with garnet core removed has the same phase topologies, with garnet's X_{Mg} and Grs isopleths systematically shifted to higher $P–T$ domains by 10–20 °C and ∼1 kbar (Supplementary Data Fig. S7). The same isopleths yield higher temperatures of 940–1000 °C at ∼8 kbar for the peak M_3 stage (Supplementary Data Fig. S7). In addition, we employ the two-feldspar thermometry of Benisek *et al.* (2004), which uses the feldspar model of Fuhrman and Lindsley (1988). Following the procedure given by Jiao & Guo (2011), the reintegrated perthite and matrix plagioclase pairs yield a minimum temperature of ≥940 °C at 8 kbar (Fig. 8d). Therefore, the peak M_3 assemblage reaches UHT metamorphism with minimum $P–T$ conditions of ∼940 °C, ∼8 kbar.

The post-peak retrograde M_4 stage is associated with final melt crystallization and the local intergrowths of biotite + quartz ± sillimanite ± plagioclase. According to the GB thermometry (Holdaway, 2000), the GASP barometry (Holdaway, 2001), and the Zr contents of matrix rutile (Fig. 8a and b), the final $P–T$ conditions of the M_4 assemblage are located at ∼5 kbar, ∼600 °C, the same as sample 16SD91. The cooling path (Fig. 10b) cuts across the biotite-in and liq-out lines, consistent with petrographic observations.

DIFFUSION MODELING

We use multicomponent diffusion modeling of garnet zonation to constrain the timescales of the $P–T$ paths (Figs 9b and 10b). The self-diffusion coefficients of Fe, Mn, Mg, and Ca in garnet are calculated using the model of Chu & Ague (2015), which considers temperature, pressure, unit-cell dimension, and oxygen fugacity. The diffusion coefficient matrix of these elements is calculated using the formalism of Lasaga (1979), which assumes an ideal garnet solution model. This simplification is commonly reasonable for the divalent cations in natural garnet (Borinski *et al.*, 2012). Diffusion equations are numerically solved by a finite-difference algorithm (Matlab code from Chu & Ague, 2015; Chu *et al.*, 2018; Faryad & Jezek, 2019). In the modeling, the $P–T$ paths (Figs 9b and 10b) are linearly discretized and diffusive relaxation is calculated at successive steps along the paths. The modeled garnets have a spherical symmetry to first order and are assumed to be sectioned through their centers.

Sample 16SD91
In sample 16SD91, the garnet mantle domains enclose kyanite and K-feldspar (Fig. 3f) from the peak M_2 assemblage, and indicate the equilibrium peak M_2 $P–T$ conditions according to the phase diagram (Fig. 9b). Phase equilibrium analyses suggest that the molar abundance of garnet reaches a maximum at the peak M_2 stage and does not grow during the retrograde M_3 and M_4 stages (Supplementary Data Fig. S4). Hence, the garnet rim
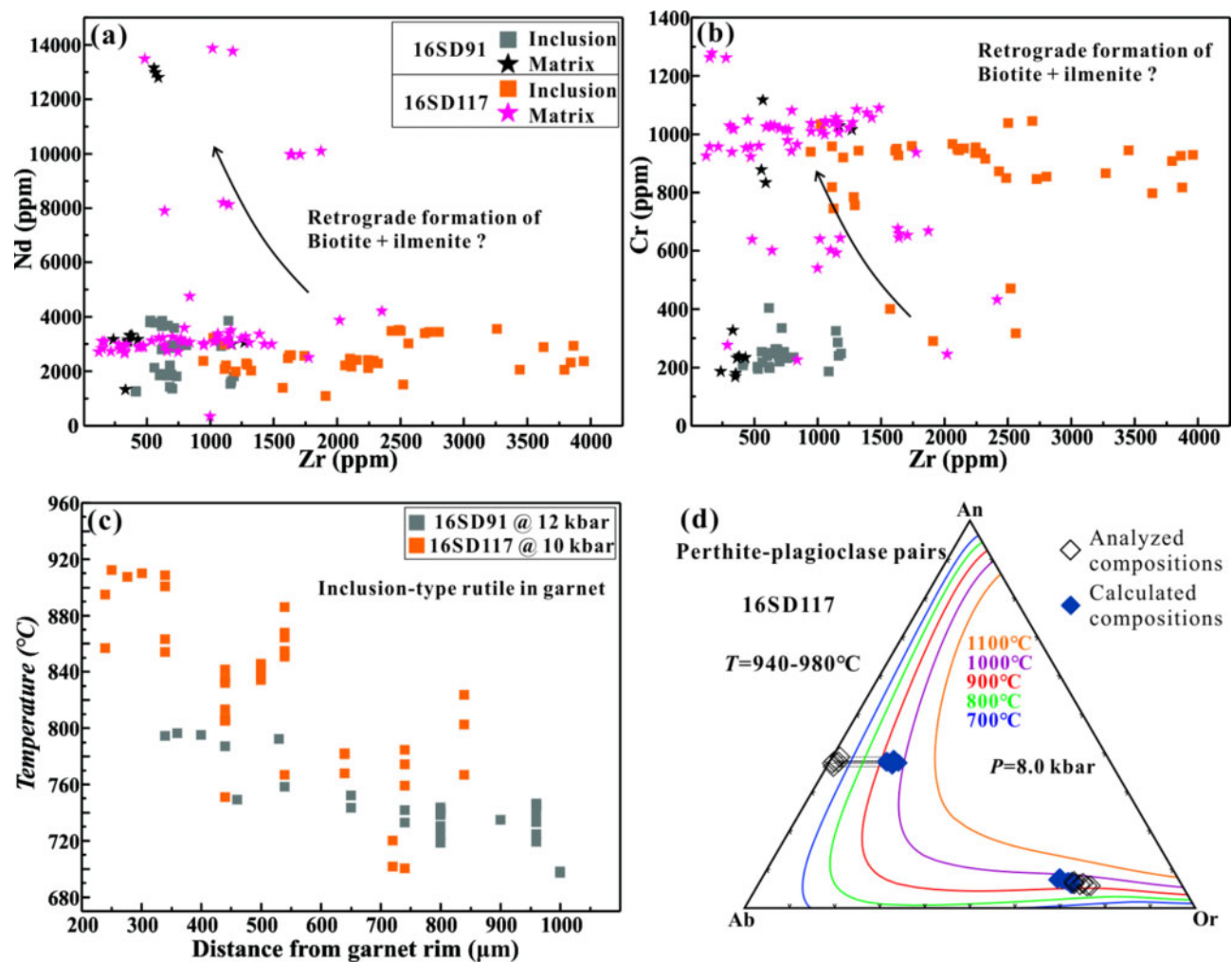
Fig. 8. (a, b) Rutile trace element variation between inclusion- and matrix-types, and (c) calculated temperature vs distance from garnet edge for isolated rutile inclusions. Pressure inputs are 12 kbar for sample 16SD91 and 10 kbar for sample 16SD117. (d) Two-feldspar thermometry of Benisek *et al.* (2004) using the solution model of Fuhrman and Lindsley (1988) for reintegrated perthite–plagioclase pairs. (See text for details.)

domains reflect post-growth diffusional modification during the retrograde metamorphism. To model the modification at the garnet rims, we use an initial homogeneous profile at the M_2 stage (Figs 9b and 11), corresponding to the relatively flat Alm, Prp, and Grs profiles in the garnet mantle domains (Fig. 6). We use an equilibrium boundary condition predicted by the phase diagram (Fig. 9b; Supplementary Data Fig. S4), and model along the decompression-cooling from the M_2 (12 kbar, 800 °C) through M_3 (8 kbar, 780 °C) to M_4 (5 kbar, 600 °C) stages (Fig. 9b). Along the $P–T$ path segments, the initial profile is modified by evolving boundary conditions in equilibrium with matrix minerals (Fig. 9b; Supplementary Data Fig. S4). The Mn profiles (Fig. 6g and h) do not display an upturn toward the rim, suggesting that the garnet is not substantially resorbed (Carlson, 2006; Ague & Carlson, 2013).

Short timescales of <5 Myr for the decompression-cooling from the M_2 to M_4 stages are required to produce a good fit to the observed retrograde profiles

(Fig. 11). Notably, the timescales of M_3–M_4 (0·5–0·8 Myr) should be several times shorter than that of M_2–M_3 (2·6–4·0 Myr) to reproduce the abrupt compositional changes near the grain boundary (Fig. 11). This implies that cooling during M_3–M_4 was faster than that during the preceding M_2–M_3 decompression, pointing to an accelerated cooling after exhumation to a mid-crustal level.

Sample 16SD117

For sample 16SD117, we consider two cases: (1) garnet rim in contact with quartz or K-feldspar; (2) garnet rim in contact with biotite. Phase equilibrium analyses suggest that the garnet core compositions mainly record a re-equilibration at the M_2 stage (Fig. 10). In the first case, the Prp or X_{Mg} profile shows a rimward increase (Fig. 7n and o) reflecting the UHT thermal excursion (M_2–M_3; Fig. 10b). We treat all the growth zonation developed during the thermal excursion as a diffusional modification. We thus use an initial profile at the
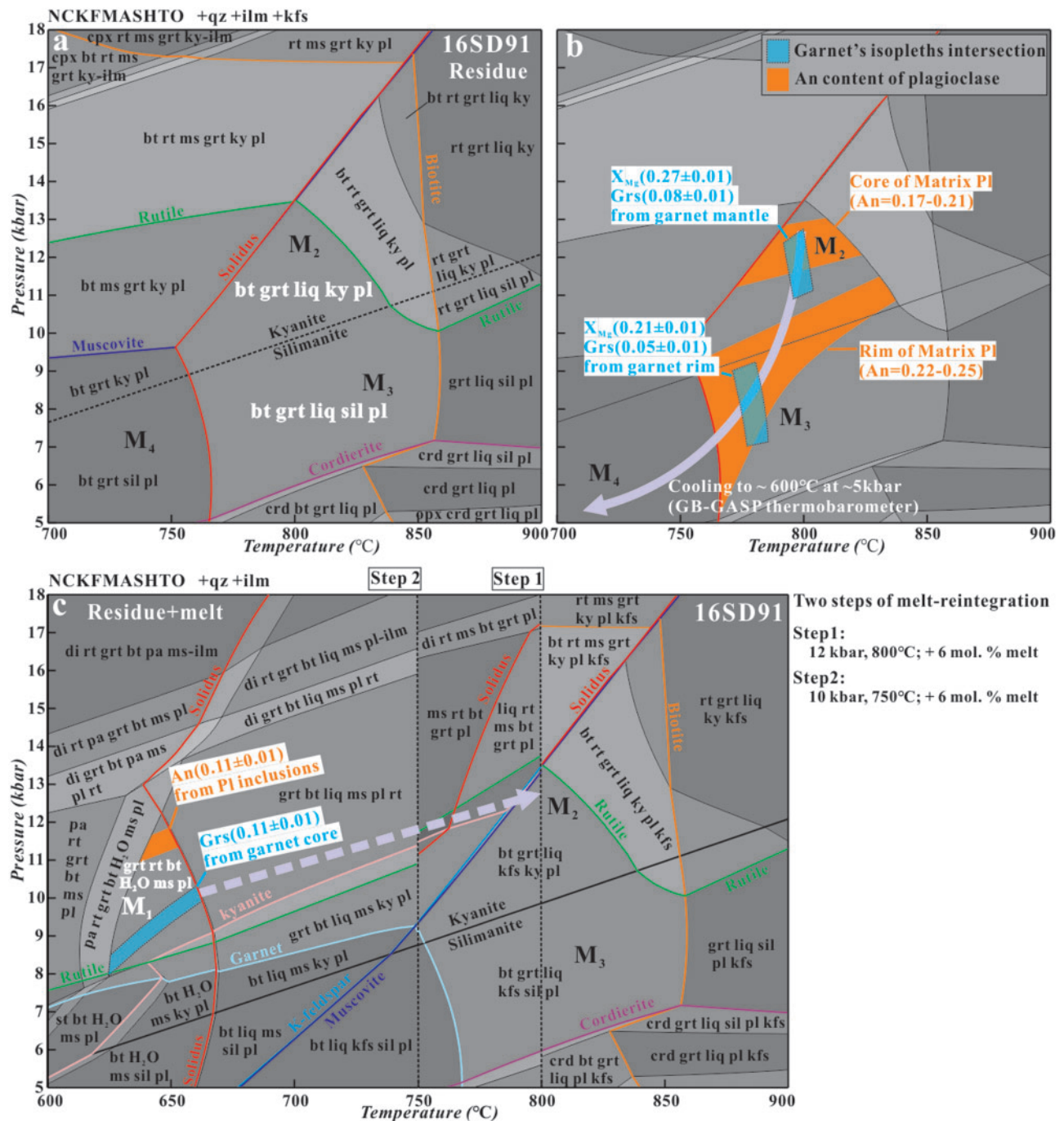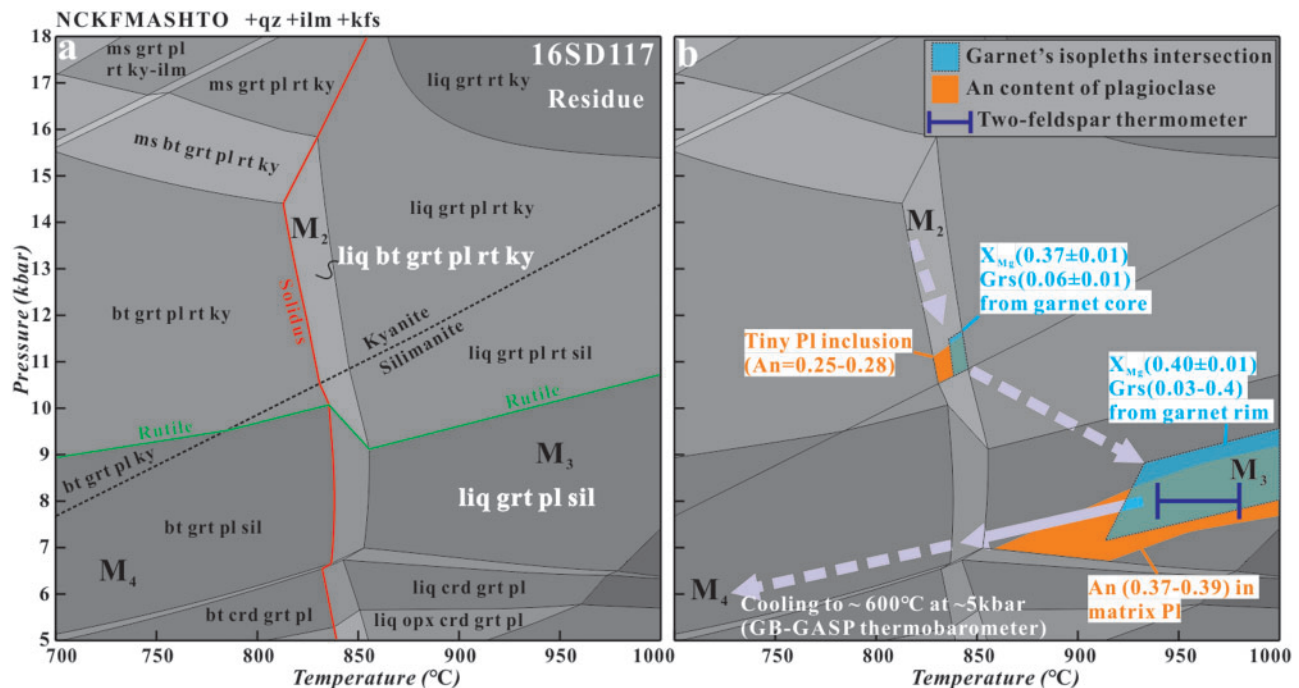
Fig. 9. (a, b) *P–T* phase diagram calculated with the measured bulk-rock composition of sample 16SD91. (a) Phase diagram labeled with modeled mineral assembles and boundaries. (b) Intersections of Grs and X_{Mg} from garnet mantle and rim domains, and isopleths of An content from matrix plagioclase, and inferred *P–T* path. It should be noted that the *P–T* conditions of the M_3 stage defined by garnet rim compositions represent a re-equilibrium condition by diffusional modification during retrograde metamorphism. The final *P–T* conditions of the M_4 stage are estimated by the GB and GASP thermobarometer (Holdaway, 2000, 2001). (c) Composite phase diagram after two steps of melt-reintegration, and the predicted subsolidus prograde M_1 assemblage. (See text for details.)

M_2 stage and its composition is determined by the phase diagram (Figs 10b and 12a, b). Given that the garnet rim is not re-equilibrated to a retrograde composition, we reasonably infer that there was no cation exchange between garnet and matrix during the cooling M_3–M_4 stages (closed system). For this case, we use two kinds of boundary conditions: (1) an equilibrium boundary during the thermal excursion (M_2–M_3; Supplementary Data Fig. S8); (2) a closed system boundary during the cooling (M_3–M_4), where the garnet rim does not communicate with the matrix, so the profile is modeled with a no-net-flux boundary setting. The

Fig. 10. *P–T* phase diagram computed using the measured bulk-rock composition of sample 16SD117. (a) Phase diagram labeled with modeled mineral assembles and boundaries. (b) Phase diagram marked with intersections of Grs and X_{Mg} from garnet core and rim domains, isopleths of An content from matrix- and inclusion-type plagioclases, and inferred *P–T* path. Also shown are the two-feldspar thermometric results (Fig. 8d). The *P–T* conditions for the M_2 stage defined by garnet core compositions reflect a re-equilibration at the M_2 stage. The final *P–T* conditions of the M_4 stage are estimated by the GB and GASP thermobarometer (Holdaway, 2000, 2001). (See text for details.)

best-fit results suggest a rapid thermal pulse (M_2–M_3) within 0·04 Myr (Supplementary Data Fig. S8), followed by a fast cooling (M_3–M_4) to ∼600 °C within 1 Myr (Fig. 12a and b).

In the second case, the garnet rim exchanges Fe and Mg cations with biotite (Fig. 7). We use an initial homogeneous profile calculated at 850 °C and ∼8 kbar, where biotite is just stable along the cooling path (Fig. 10b). We consider only the Mg–Fe exchange between garnet and biotite during the cooling (850–600 °C), and follow the general procedure proposed by Spear (1991) and Sorcar *et al.* (2014). The grain sizes of garnet and biotite are determined from thin sections (Fig. 4b and f), and the boundary condition at the biotite–garnet interface (Fig. 12d1) is estimated by the Fe–Mg geothermometer of Ferry & Spear (1978). We calculate the diffusive penetration of the evolving boundary conditions at a variety of cooling rates (Fig. 12c1). The best-fit timescales are shown in Fig. 12c and d. Notably, using a constant cooling rate cannot reproduce the observed retrograde profiles, and nonlinear cooling histories with a faster rate at high temperatures yield a much better fit (Fig. 12c and d). The timescales for the cooling (850–600 °C) are longer (2·32–4·0 Myr; Fig. 12c and d), but of the same order of magnitude as the modeling results in the first case (Fig. 12a and b). The longer best-fit timescales shown in Fig. 12c2 and c3 are attributed to oblique sectioning that can overestimate timescales (Ague & Baxter, 2007; Chu *et al.*, 2017).

For the second case, we also test the dependence of modeled timescales on initial profiles. We start from the initial profile applied in the first case. Through the thermal spike (M_2–M_3–850 °C), we use an equilibrium boundary condition (Fig. 10b; Supplementary Data Fig. S6) and calculate a series of diffusion profiles. Then we use the modeled profiles as initial profiles for the cooling (850–600 °C) and follow the same procedure for the local Mg–Fe exchange between garnet and biotite (Fig. 12d1). The modeled profiles after the thermal excursion (M_2–M_3; 0·04 Myr) and the cooling (M_3–850 °C; 0·6 Myr) are shown in Supplementary Data Fig. S9. The final modeled profiles after the cooling from 850 to 600 °C are given in Supplementary Data Fig. S10, which yield almost identical timescales to the simple flat initial profile.

ZIRCON, MONAZITE, AND RUTILE GEOCHRONOLOGY

Zircon, monazite, and rutile SIMS U–Pb dating was conducted on the pelitic granulites. The analytical conditions are described in the Supplementary Material A3. All the data are given in Supplementary Data Tables T2–T4. Mean ages for pooled U/Pb or Pb/Pb analyses are quoted with 95 % confidence. The ages, in combination with cathodoluminescence (CL) and BSE characteristics, inclusions, rare earth elements (REE) analyses,

and closure temperature, help to place constraints on the timing of metamorphic events.

Zircon geochronology

CL images reveal two types of zircons: (1) the dominant grains, which have a CL-darker core and a thin brighter rim; (2) unzoned to sector zoning zircon crystals. The CL-brighter rims are commonly multifaceted, unzoned to sector zoned. The core–rim boundaries are curved and show dissolution textures (Fig. 13a; spots 4 and 15), probably suggesting that the rims are newly grown metamorphic zircons (e.g. Zhao *et al.*, 2015). A total of 27 analyses were performed on 27 zircons, of which 12 analyses were on unzoned crystals, 14 analyses were on CL-darker cores, and one analysis was on CL-brighter rims (Fig. 13a; spot 13). Among the 14 analyses on cores, five spots have much higher Th/U ratios (0·14–0·32) and more variable $^{206}Pb/^{207}Pb$ dates of 1900–2056 Ma than other spots (Fig. 14a; spots 2, 7, 9, 22, and 24), and one spot (spot 11) has high common Pb. These analyses were excluded from the age calculation. The remaining analyses are characterized by low Th/U ratios (<0·07), and 11 concordant analyses give a weighted mean $^{206}Pb/^{207}Pb$ age of 1871 ± 9 Ma (Fig. 14a).

No index metamorphic minerals were identified within the zircon grains. To relate the age to metamorphic stages, we additionally analyzed the REE contents of zircon and garnet using LA-ICP-MS (Supplementary Data Tables T5 and T6). The domains of zircon grains (unzoned zircon crystals) chosen for REE analyses are the same as those where the U–Pb dating was conducted. A noteworthy feature of the zircon grains is the enrichment of Tm, Yb, and Lu, instead of a flat heavy REE pattern, and meanwhile the negative Eu anomaly is reduced (Supplementary Data Fig. S11). The peculiar REE patterns in zircon imply some garnet resorption in the presence of melt, so the unzoned zircons were formed during exhumation and cooling stages where garnet mode decreases (Supplementary Data Fig. S4). Their indistinguishable ages within analytical uncertainty corroborate a fast exhumation–cooling process and are consistent with the diffusion modeling results (Fig. 11).

Zircon grains from sample 16SD117 have similar CL features to those of 16SD91. A total of 26 spots were analyzed on 26 zircon grains, of which 13 analyses were on CL-darker cores, two analyses were on CL-brighter rims, and 11 analyses were on unzoned crystals. The analyses on cores have slightly higher U and Th contents, but consistently low Th/U ratios (<0·08), suggesting that these cores were completely reset by high-grade metamorphism (Vavra *et al.*, 1996; Schaltegger *et al.*, 1999; Geisler *et al.*, 2007; Zhao *et al.*, 2015). The long re-equilibration at the M₂ stage may favor such a complete reset. The analyses on unzoned crystals and CL-brighter rims have variable Th/U ratios, and notably some are in excess of 0·1 (Fig. 13b; Supplementary Data Table T2; spots 7, 12, 18, 19, and 20). Metamorphic zircons with Th/U > 0·1 are commonly reported in high- to

ultrahigh-temperature pelitic granulites (Vavra *et al.*, 1996; Schaltegger *et al.*, 1999; Harley *et al.*, 2007; Rubatto, 2017). Inclusions of sillimanite and rutile were identified in the CL-brighter rims (Fig. 13b; spot 21) and unzoned zircon crystals (Fig. 13b; spots 18 and 23). We therefore conclude that these zircon grains formed in the sillimanite-stability field, close to the peak UHT conditions (M₃ stage). Despite the variations in chemistry and inclusions, the 26 spots analyzed have overlapping $^{206}Pb/^{207}Pb$ dates, consistent with the defined short-lived thermal excursion. Fifteen concordant analyses give a concordia age of 1847 ± 8 Ma and a weighted mean $^{206}Pb/^{207}Pb$ age of 1851 ± 8 Ma (Fig. 14b).

Monazite geochronology

The monazite grains are unzoned in BSE images (Fig. 13c and d) with inclusions of quartz, plagioclase, K-feldspar, and sillimanite (Fig. 13c and d). The plagioclase inclusions chemically resemble those of retrograde intergrowths, suggesting monazite formation during cooling (M₃–M₄, Figs 9b and 10b). For sample 16SD91, a total of 23 analyses were made on 22 monazite grains. These analyses are concordant and define a concordia age of 1865 ± 6 Ma and a weighted mean $^{206}Pb/^{207}Pb$ age of 1870 ± 4 Ma (Fig. 14c). For sample 16SD117, a total of 23 analyses were performed on 20 grains. Three spots (spots 16, 17 and 22; Supplementary Data Table T3) were excluded because they have higher Th contents and lower $^{207}Pb/^{206}Pb$ ages than other spots. The remaining 20 spots yield a concordia age of 1848 ± 7 Ma and a weighted mean $^{206}Pb/^{207}Pb$ age of 1852 ± 5 Ma (Fig. 14d).

Rutile geochronology

Rutile grains of sample 16SD91 are homogeneous in BSE images (Fig. 13e). A total of 25 analyses were made on 22 grains or fragments. Three analyses (spots 4, 14 and 20; Supplementary Data Table T4) were excluded owing to high common Pb. The remaining 22 analyses have U contents of 3–61 ppm and define a discordia with an upper intercept age of 1825 ± 16 Ma (Fig. 14e). Nine concordant analyses yield a weighted mean $^{206}Pb/^{207}Pb$ age of 1823 ± 17 Ma (Fig. 14e). Rutiles from sample 16SD117 are larger in size (200–300 μm; Fig. 13f), and some have Zr-bearing oxide exsolutions (Fig. 13f; spots 12 and 13) in response to cooling from higher temperatures. Twenty-seven spots were analyzed on BSE-homogeneous domains. Two analyses (spots 10 and 24) have much younger $^{207}Pb/^{206}Pb$ dates (<1760 Ma), presumably owing to U–Pb remobilization by a later thermal process. The remaining 25 analyses define a discordia with an upper intercept age of 1813 ± 6 Ma, and 20 concordant analyses give a concordia age of 1814 ± 6 Ma and a weighted mean $^{206}Pb/^{207}Pb$ age of 1814 ± 3 Ma (Fig. 14f). We note that the U contents of rutile grains in sample 16SD91 are much lower than those of sample 16SD117 (Fig. 14e and f). The study of Li *et al.* (2011a) revealed that low-U
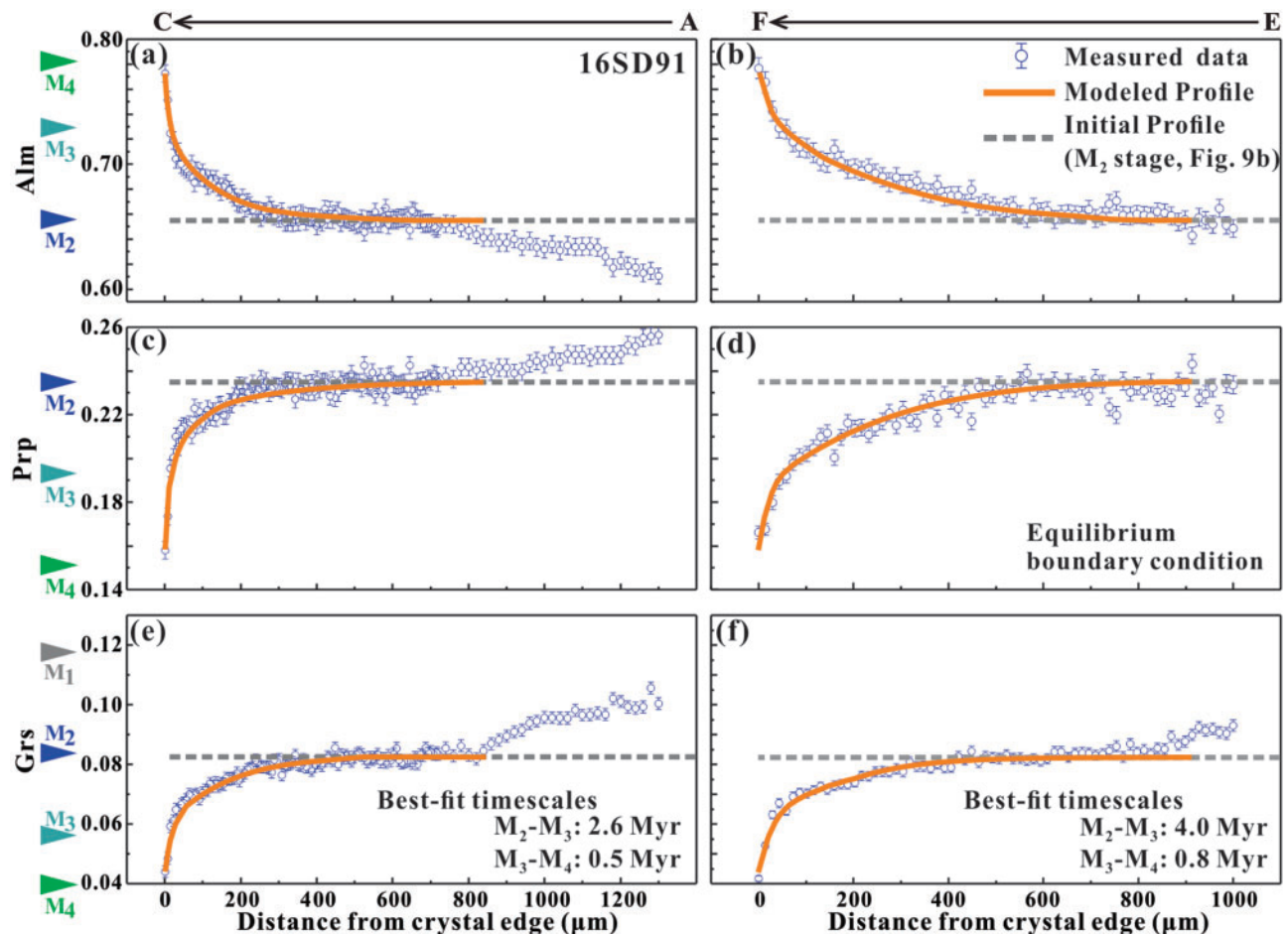
Fig. 11. Garnet multicomponent diffusion modeling for sample 16SD91. It should be noted that the timescales for M_3–M_4 should be several times smaller than that of M_2–M_3 to obtain a good fit. (See text for details.)

rutile tends to yield more scattered U–Pb ages, which could explain the larger uncertainty of rutile U–Pb ages of sample 16SD91 (Fig. 14e; Supplementary Data Table T4).

Experiments suggest that the closure temperature of the rutile U–Pb system occurs at ~600 °C (e.g. Cherniak, 2000). Although rutile grew during high-grade metamorphisms, rapid cooling rates of rocks require that rutile U–Pb ages reflect a cooler ($T < 500$ °C) part of retrograde metamorphism (e.g. Li *et al.*, 2003). These constraints are consistent with results from other studies that suggest that experiments have significantly overestimated the retention of Pb in rutile (e.g. Mezger *et al.*, 1989; Meinhold, 2010). Therefore, the rutile ages in this study are interpreted to date the time when rocks cooled to <500 °C.

DISCUSSION

Assumptions and uncertainties of diffusion modeling

The diffusion modeling has several key assumptions. First, for equilibrium boundary conditions, garnet boundaries are assumed to always reach equilibrium with matrix minerals or biotite during the *P–T* evolutions (Figs 9b and 10b).

This is a strong assumption that was also included in previous simulations (Spear, 1991; Gaidies *et al.*, 2008; Caddick *et al.*, 2010; Chu *et al.*, 2018). Such an assumption is underpinned by faster intergranular diffusion than intracrystalline diffusion at amphibolite- or granulite-facies conditions (e.g. Gaidies *et al.*, 2008; Chu *et al.*, 2018). Second, the initial profiles are assumed to be homogeneous at the M_2 stages for both samples (Figs 11 and 12). Our modeling code allows an arbitrary initial profile to evolve during an arbitrary thermal history (e.g. Supplementary Data Fig. S10). If the initial profiles are gradational towards the subsequent M_3–M_4 stages, diffusion modeling using a homogeneous initial profile at the M_2 stage would tend to overestimate the timescales of the M_3–M_4 stages (Ague & Baxter, 2007; Sorcar *et al.*, 2014). Third, the modeling assumes that garnet is center-cut and measured profiles are perpendicular to the grain boundaries. Diffusion modeling to fit inclined or off-center analyses would yield a false, longer timescale (Ague & Baxter, 2007; Chu *et al.*, 2017). This effect is demonstrated in Fig. 12c2 and c3, where the smaller garnet that was cut off-center yields a longer timescale.

A fourth limitation is the neglect of garnet growth or resorption. For sample 16SD91, we model the largest
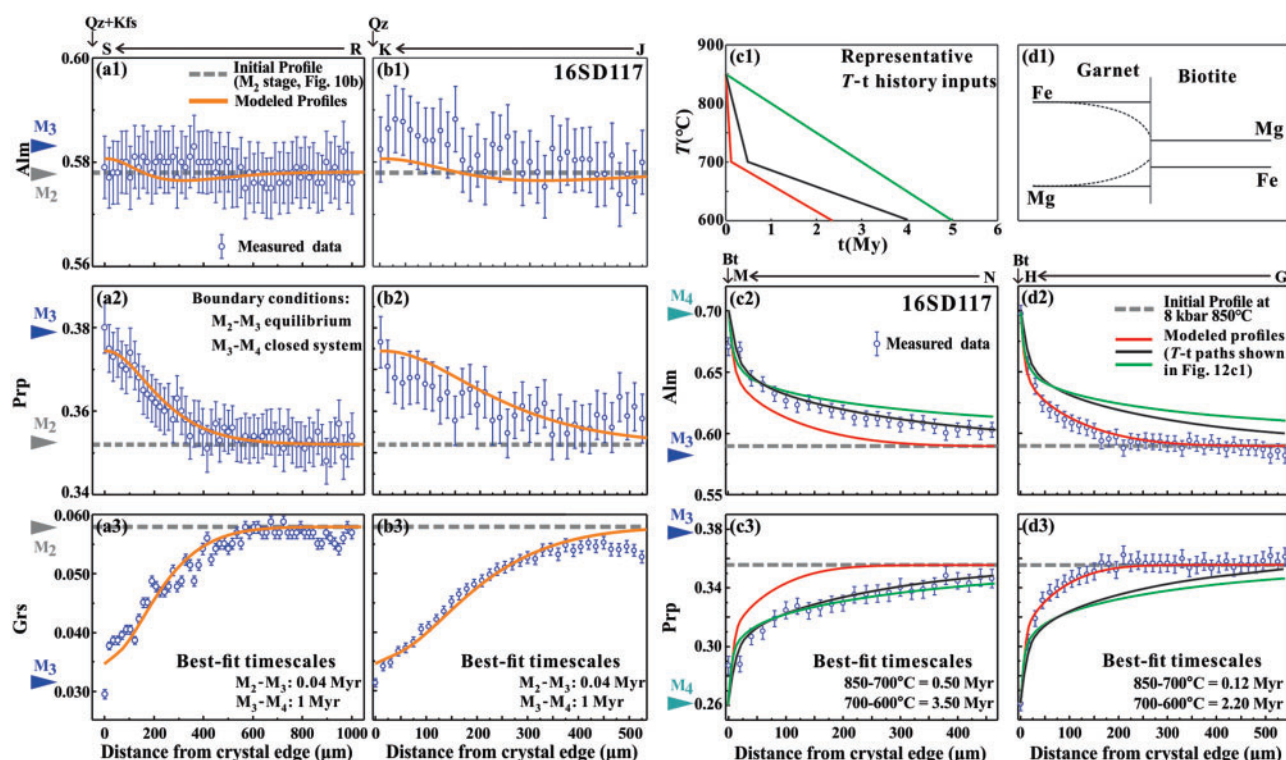
Fig. 12. Garnet multicomponent diffusion simulation for sample 16SD117. (a, b) Diffusion modeling conducted for the garnet rim in contact with quartz and K-feldspar. An equilibrium boundary condition is applied for the thermal excursion (M_2–M_3), and a closed system boundary condition is used for the cooling (M_3–M_4). (c, d) Diffusion modeling for the garnet rim in contact with biotite. (c1) Representative cooling history inputs. (d1) Schematic diagram showing the Fe–Mg diffusive exchange between garnet rim and biotite. (c2, d2; c3, d3) Representative modeling results with the thermal history inputs shown in (c1). It should be noted that modeled profiles using a constant cooling rate match only the zoning pattern near garnet edges. Nonlinear cooling with a faster rate at high temperatures better fits the measured profiles. (See text for details.)

garnet observed, and the Mn zonings do not display an upturn toward the rims (Figs 5b and 6g, h), implying that the rims are not significantly resorbed (Carlson, 2006; Ague & Carlson, 2013). The initial profile is set at the peak M_2 stage, and the garnet does not grow during subsequent retrograde stages. Hence, ignoring garnet growth is reasonable in modeling the garnet retrograde profiles of sample 16SD91 (Fig. 11). For sample 16SD117, garnet might grow during the thermal excursion (M_2–M_3), even though phase equilibrium analyses indicate largely constant garnet modes (Supplementary Data Fig. S6). The isolated rutile inclusions near garnet rims record higher temperatures than the M_2 stage, approaching the thermal peak M_3 (Fig. 8c), so garnet possibly grew and captured the rutile inclusions during the thermal excursion. We note that the growth zonation during the thermal excursion better approaches the observed profiles (Fig. 12a and b; Supplementary Data Fig. S7). By assuming a flat initial condition at the M_2 stage, we enlarge the diffusion lengthscales of the thermal excursion and subsequent cooling, and thus overestimate their timescales. For the cooling path (850–600 °C), we ignore biotite growth in calculating the Fe–Mg exchange between garnet and biotite (Fig. 12c and d). This might compromise our cooling history calculations. Nevertheless, biotite is minor in thin section

(Fig. 4a) and its volume percentage remains nearly constant during the cooling (Supplementary Data Fig. S6).

A fifth assumption is that no grain-scale stress variation could slow down diffusion driven by chemical potential gradients. The stress anomaly at compositional contrasts within garnet was proposed by Baumgartner (2010), but this mechanism is unlikely in our samples. Our multicomponent diffusion yields consistent timescales, independent of diffusing components, and we do not observe dense fractures (Whitney, 1996; Broadwell *et al.*, 2019) or highly asymmetric growth zonation (Zhong *et al.*, 2017) that would indicate large intracrystalline pressure variations (10–12 kbar; Baumgartner, 2010). Taking the garnet from sample 16SD91 as an example (Fig. 5a–d), the discordant compositional zonings for Ca, Mg, and Fe can be well explained by differential diffusion, but are incompatible with the intracrystalline pressure variation. Thus, we reasonably preclude the effect of grain-scale stress variations in our samples.

The modeling results are subject to uncertainties mainly derived from (1) the modeled *P*–*T* paths and compositional isopleths used to set boundary conditions, and (2) the diffusion model of Chu & Ague (2015). The relative uncertainties of our modeled *P*–*T* paths and compositional isopleths are of the order of ±10 °C and
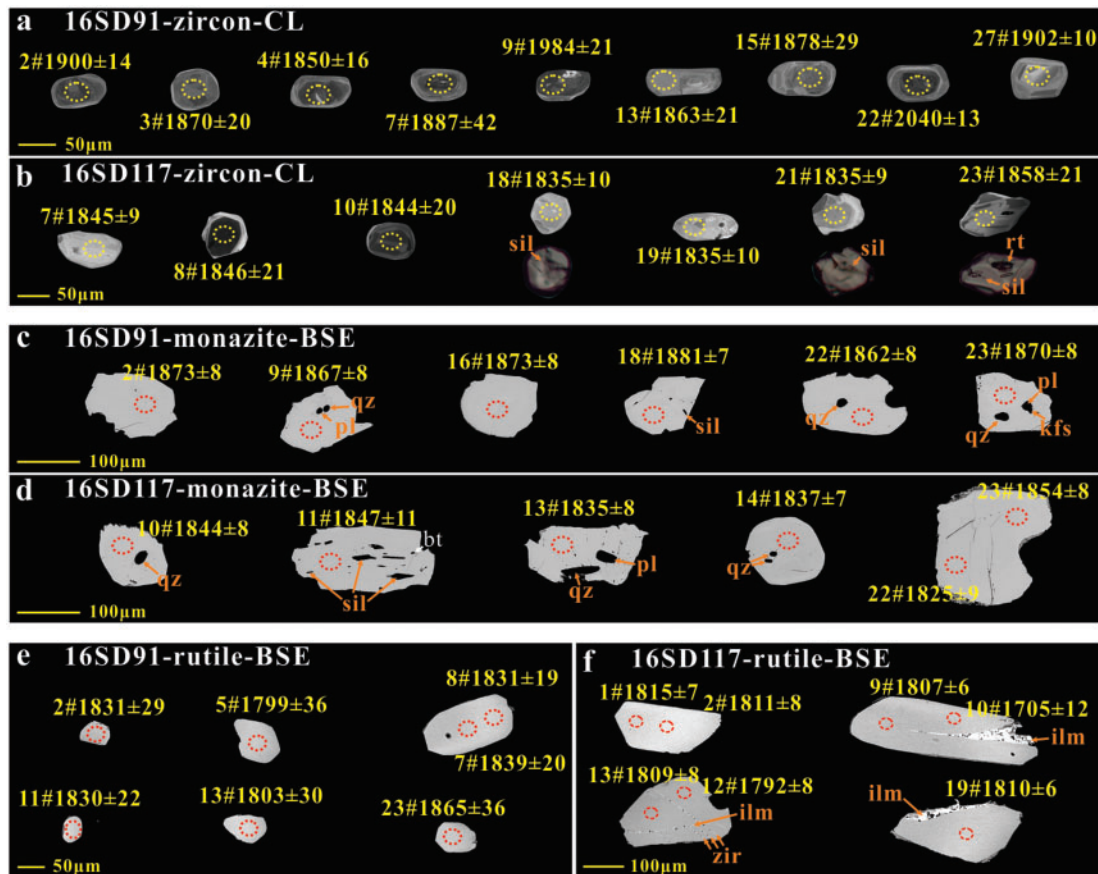
Fig. 13. (a, b) Representative CL images of zircon grains. The enclosed inclusions of rutile and sillimanite should be noted. (c, d) Representative BSE images of monazite grains. The enclosed inclusions of sillimanite, plagioclase, and K-feldspar should be noted. (e, f) Representative BSE images of rutile grains. The rutile grain containing zircon exsolutions should be noted. Yellow or orange dashed ellipses represent the analyzed spots with a size of $20 \times 30\,\mu m$. Yellow numbers denote the spot number and corresponding $^{207}Pb/^{206}Pb$ age with error (1σ).

$\pm 2\,kbar$ (2σ) based on the phase diagrams calculated with measured bulk-rock compositions (Figs 9 and 10; Supplementary Data Figs S4 and S6). These uncertainties would propagate to ± 0.1 order of magnitude for the relative uncertainties of timescales. The *P–T* paths in the phase diagrams calculated with bulk compositions with garnet core removed shift systematically to higher *P–T* domains by 5–20 °C and 1–2 kbar (Supplementary Data Figs S5 and S7). Using these *P–T* paths and isopleths as boundary conditions would yield shorter timescales by about 0.05–0.2 order of magnitude. The relative uncertainties of the diffusion model are typically within ± 0.3 order of magnitude (Chu & Ague, 2015). We test the sensitivity of modeling results to timescales (Fig. 12c and d; Supplementary Data Fig. S10), and a longer duration by less than 0.3 order of magnitude produces notable differences. Thus, the relative uncertainty of the modeled timescales is probably within 0.3–0.4 order of magnitude. Besides, diffusion experiments on garnet were conducted in nominally anhydrous conditions. The recent study by Zhang *et al.* (2019) has demonstrated enhanced rates of Fe–Mg inter-diffusion by increasing water contents. Using the increased

diffusion coefficients owing to minor water contents in our samples will yield shorter durations.

In summary, given the assumptions and uncertainties, the modeled timescales are conservative and should be regarded as upper-limit estimates.

Metamorphic *P–T–t* evolution and rates of metamorphism

Considering the error inherent in the reproducibility of SIMS U–Pb geochronology (1–2 %; Li *et al.*, 2015), we set an overall conservative uncertainty of $\pm 1\%$ on all zircon, monazite, and rutile U–Pb ages when correlating them to metamorphic *P–T* paths (Fig. 15). We note that the uncertainty of $^{207}Pb/^{206}Pb$ ages could be smaller than 1 %, depending on the complexity of measured samples (e.g. Fig. 14e). The two pelitic granulites record clockwise but distinct metamorphic *P–T–t* evolution and timescales. The one from the Taipingzhuang area is characterized by peak HPG metamorphism of $\sim 12\,kbar$ and 800 °C, followed by a decompression-cooling to $\sim 5\,kbar$ and ~ 600 °C (Figs 9b and 15a). Zircon and monazite yield indistinguishable ages of $1870 \pm 19\,Ma$ (an overall uncertainty of $\pm 1\%$). The peculiar REE
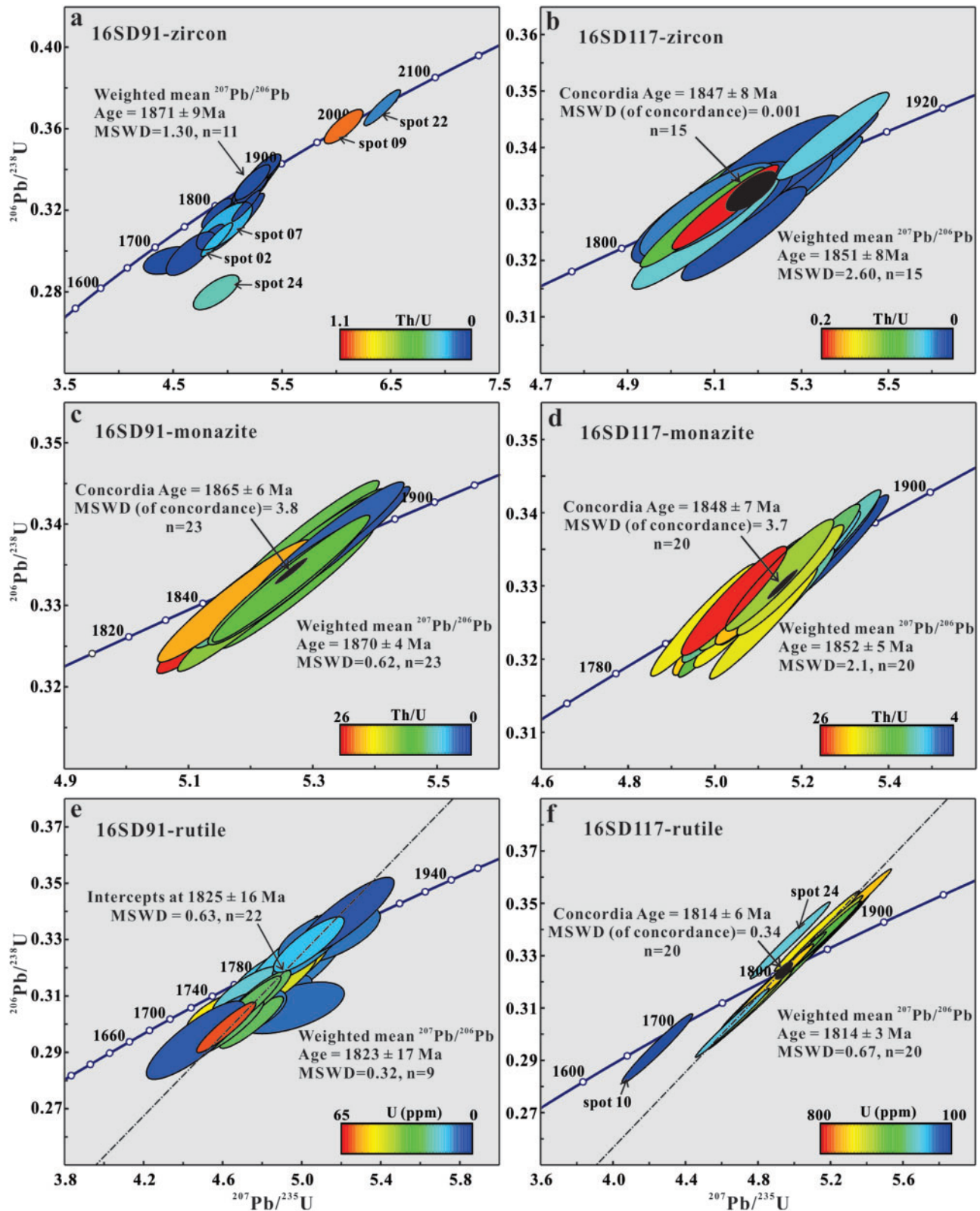
Fig. 14. (a, b) Zircon, (c, d) monazite, and (e, f) rutile U–Pb concordia diagrams, contoured with Th/U ratios, Th/U ratios, and U contents, respectively.

patterns in zircon (Supplementary Data Fig. S11), in concert with inclusions within monazite, suggest 1870 ± 19 Ma as the timing of the decompression-

cooling (M_2–M_4 stages; Fig. 15a), probably accompanying melt crystallization (Kelsey & Powell, 2011; Kohn *et al.*, 2015). This *P–T–t* path is consistent with previous
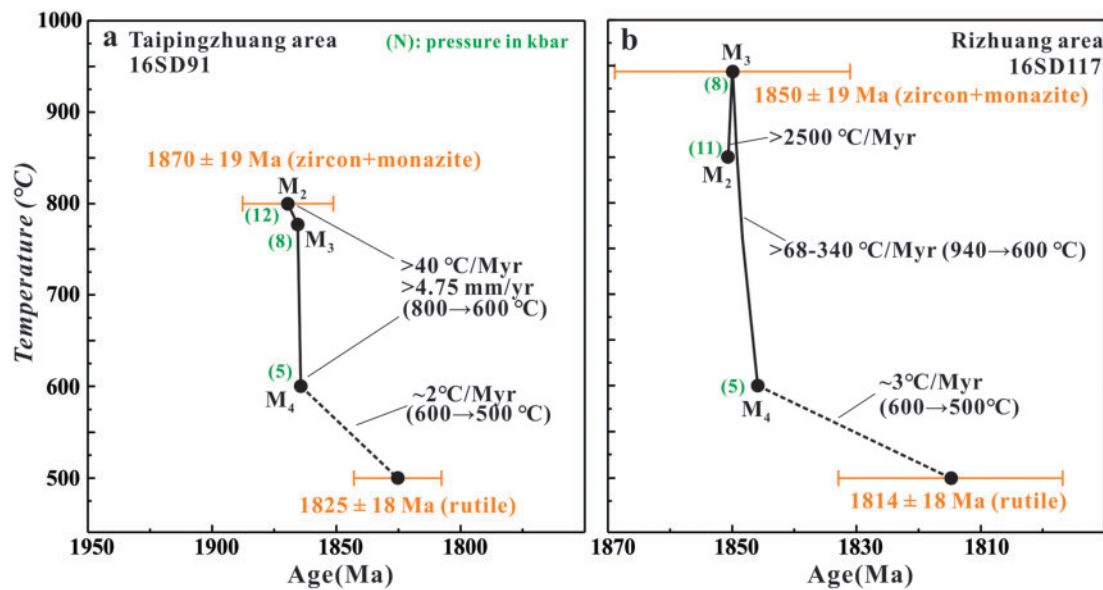
Fig. 15. Metamorphic *P–T–t* paths and rates retrieved from pelitic granulites in the Taipingzhuang and Rizhuang areas. It should be noted that an overall conservative uncertainty of ±1% is set on zircon, monazite, and rutile U–Pb ages, although the errors of ^{206}Pb/^{207}Pb ages are probably smaller than 1%, depending on the complexity of measured samples.

studies in the Taipingzhuang area (Zhou *et al.*, 2008*b*; Tam *et al.*, 2012*b*). At 1825 ± 18 Ma, the pelitic granulite cooled to temperatures below ∼500°C (Fig. 15a). Diffusion modeling further reveals that the decompression-cooling is rapid within ∼5 Myr (Fig. 11), pointing to fast exhumation and cooling rates of >40°C Ma^{-1} and >4·75 mm a^{-1} (Fig. 15a). The fast rates defined are consistent with the preservation of multistage mineral assemblages and the zircon heavy REE characteristics.

In comparison, the granulite (sample 16SD117) from the Rizhuang area is characterized by a thermal excursion from ∼11 kbar, ∼840°C to peak UHT metamorphism of ∼940°C, ∼8 kbar, followed by a near isobaric cooling to ∼600°C, ∼5 kbar (Figs 10b and 15b). Zircon and monazite record a consistent age of 1850 ± 19 Ma (Fig. 15b), and some metamorphic zircons have high Th/U ratios >0·1. In a pelitic system, the absence or dissolution of monazite at high-temperature to UHT conditions can produce metamorphic zircons with a high Th/U ratio >0·1 (Rubatto, 2017; Yakymchuk *et al.*, 2018). Therefore, the consistent age may imply a rapid cooling process from the thermal peak that occurred at *c.* 1850 ± 19 Ma (Fig. 15b). At 1814 ± 18 Ma, the pelitic granulites cooled to temperatures below ∼500°C (Fig. 15b). Garnet diffusion simulation suggests that the thermal excursion is transient within 0·04 Myr, followed by a fast cooling process to ∼600°C within 1–5 Myr. These constraints define a short-lived UHT metamorphism with a heating rate of >2500°C Ma^{-1}, followed by fast cooling rates of >68–340°C Ma^{-1} (Fig. 15b). Such short timescales favor the preservation of kyanite (Fig. 4b and c) and rutile (Fig. 4d) from the lower-pressure UHT metamorphism, and are consistent with the zircon and monazite ages.

Potential mechanism for the rapid decompression-cooling

The HPG pelitic granulites from the Taipingzhuang area trace a clockwise *P–T–t* path that is similar to those predicted from numerical geodynamic modeling and inferred from metamorphic petrology of rocks in modern convergent orogens (e.g. England & Thompson, 1984; Thompson & England, 1984; Beaumont *et al.*, 2004, 2006; Wang *et al.*, 2017). The age of 1870 ± 19 Ma for the decompression-cooling is broadly coeval with adakitic granites emplaced across the Jiao-Liao-Ji orogenic belt. Geochemical data indicate that these adakitic granites were formed by partial melting of thickened lower crust (Xu & Liu, 2019). This observation suggests that the tectonic environment of the decompression-cooling is syn-collisional.

Regional structural analysis by Li *et al.* (2012) supports syn-collisional exhumation of the HPG granulites in the Taipingzhuang area. Two major ductile shear zones (the Tading–Xiadian and Taipingzhuang ductile shear zones; Fig. 1c) border the Archean basement and overlying Jingshan Group (Li *et al.*, 2012). The associated shearing might be responsible for the fast exhumation and cooling of the HPG granulites, in a similar manner to the syn-collisional tectonic extrusion initially proposed for the Greater Himalayan Crystalline Complex (Beaumont *et al.*, 2004; Jamieson *et al.*, 2004). This compressional extrusion model predicts the juxtaposition of extruded high-grade crustal rocks with lower-grade rocks in the vicinity of the erosion front (Beaumont *et al.*, 2004; Wang *et al.*, 2013). This setting is well reflected in the Jingshan Group, particularly around the Taipingzhuang area, where minor greenschist-facies pelitic units are exposed in localities close to the HPG pelitic granulites. Furthermore, the

numerical thermo-rheological simulation conducted by Schulmann *et al.* (2002) has shown the ability of tectonic extrusion in transporting thermally softened, thickened lower-crustal segments into cold upper crust within a short time (<7 Myr), which then resulted in fast cooling (Sorcar *et al.*, 2014). Such an accelerated cooling during exhumation is also well reflected by our diffusion modeling (Fig. 11). Therefore, we infer that syn-collisional exhumation at 1870 ± 19 Ma, most probably through tectonic extrusion, led to the rapid exhumation and cooling (Figs 15a and 16a), in a process similar to that for the Greater Himalayan Crystalline Complex.

Possible thermal regime of the short-lived UHT metamorphism

The short-lived UHT metamorphism requires a local and transient heat source (Guevara *et al.*, 2017; Viete & Lister, 2017; Chu *et al.*, 2018) beyond conductive heating in thickened crust (Thompson & England, 1984; Clark *et al.*, 2011; Guevara *et al.*, 2017). The *c.* 1850 Ma UHT metamorphism is synchronous with the emplacement of mafic dykes in the Rizhuang area (Dong *et al.*, 2011; Fig. 2a and b; Supplementary Data Fig. S2). The mafic dikes intruded in response to asthenosphere upwelling and basaltic underplating during post-collisional extension (see the review by Liu *et al.*, 2015*c*; Fig. 16b). The basaltic underplating may provide the ultimate heat budget for the extensive low- to medium-pressure (LMP) granulite-facies metamorphism in the Rizhuang area (Liu *et al.*, 2011*b*, 2014, 2015*c*). In general, underplating of mafic magmas at the base of the crust would establish a long thermal interval on a regional scale (Peressini *et al.*, 2007; Guevara *et al.*, 2017). Nevertheless, the *c.* 1·85 Ga mafic intrusions are not homogeneously distributed within the Rizhuang area, and are rare or absent in the Taipingzhuang area (Figs 1c and 16b), which can be attributed to the asymmetric magmatic underplating during the extension (Li *et al.*, 2011*b*; Fig. 16b). Local emplacement of smaller bolides of mafic dikes related to more voluminous magmatic underplating at the base of the crust can serve as a transient heat input for a metamorphic thermal peak (Ague & Baxter, 2007; Clark *et al.*, 2014; Guevara *et al.*, 2017; Chu *et al.*, 2018). The transient UHT peak directly baked by the mafic intrusions overprints the regional background of high-temperature metamorphism in response to the larger-scale underplating (Fig. 16b).

In addition to the common genesis of UHT granulites in arcs to back-arcs proposed by Brown (2006) and long-lived UHT metamorphism (Clark *et al.*, 2011; Kelsey & Hand, 2015; Harley, 2016), UHT metamorphism can transiently occur in an extensional setting, as exemplified by the youngest Seram UHT granulites identified at the Earth's surface (Pownall *et al.*, 2014). Similar to our case study, transient UHT metamorphism at *c.* 1·85 Ga caused by mafic magmas during extension is also recorded in sapphirine-bearing metapelites from the Khondalite Belt within the north of the NCC (Fig. 1b;

Jiao *et al.*, 2015). The metamorphic zircons from the three Paleoproterozoic belts within the NCC record broadly four age group peaks at *c.* 1950 Ma, *c.* 1920 Ma, *c.* 1870 Ma, and *c.* 1850 Ma (e.g. Peng *et al.*, 2014), suggesting an overall long-lived collisional orogenesis (Zhou *et al.*, 2017) or a more dynamic accretionary orogenesis with cycles of 'tectonic swtiching' between lithospheric-scale shortening and extension (Collins, 2002). The transient UHT metamorphism at *c.* 1·85 Ga represents a thermal pulse or pulses of the ancient orogenesis.

Implications for Paleoproterozoic tectonic regimes

A general consensus has been reached that the JLJB is a Paleoproterozoic (1·95–1·80 Ga) orogenic belt that formed during the collisional assembly of the NCC within the supercontinent Columbia (Fig. 1a; e.g. Zhao & Zhai, 2013; Liu *et al.*, 2015*a*; Xu & Liu, 2019). The thermal peak defined (∼12 kbar, ∼800 °C) from HPG pelitic granulites shows the transport of sedimentary protoliths to a deep crustal level (∼40 km). Such a deep burial of sedimentary rocks followed by exhumation is mediated by plate-tectonic-like processes (Brown, 2006; Tam *et al.*, 2012*b*; Zou *et al.*, 2017).

The timescale information (exhumation and cooling rates) of ancient HPG rocks can provide insights into the nature of ancient tectonic regimes (Willigers *et al.*, 2002; Zhai, 2009; Chowdhury & Chakraborty, 2019). The HPG granulites from the Taipingzhuang area experienced a fast decompression-cooling (>4·75 mm a^{-1}, >40 °C Ma^{-1}) in response to syn-collisional tectonics, most probably through tectonic extrusion. The Higher Himalayan Crystalline Complex arguably serves as a fitting modern analog for our Paleoproterozoic case. Similar 1·8–2·1 Ga high-*P* rocks that document fast exhumation and cooling are also found in other Paleoproterozoic belts worldwide, such as the Snowbird tectonic zone, western Canadian Shield (Baldwin *et al.*, 2007) and the Usagaran Orogen, Tanzania (Collins *et al.*, 2004). These Paleoproterozoic fast rates are broadly synchronous with the first global records of high-pressure metamorphism with low thermal gradients (<10 °C km^{-1}) recognized in Paleoproterozoic orogenic belts (Fig. 1a; Ganne *et al.*, 2012; Glassley *et al.*, 2014; Weller & St-Onge, 2017; Xu *et al.*, 2018*a*). Such low thermal gradients are suggestive of cold subduction processes, a diagnostic feature of modern plate tectonics (Brown, 2006; Stern, 2005). These comparative tectonics and rock records including subduction with low thermal gradients and collision-driven fast exhumation and cooling collectively imply that modern plate tectonics possibly had been operative during the Paleoproterozoic era (2·1–1·8 Ga). The primary reason for the possible operation of modern plate tectonics during 2·1–1·8 Ga may be linked to the enhanced mantle cooling at *c.* 2·1 Ga (Liu *et al.*, 2019).

The dichotomy of thermal regimes (UHT and HPG) has been interpreted to mark the onset of Paleo
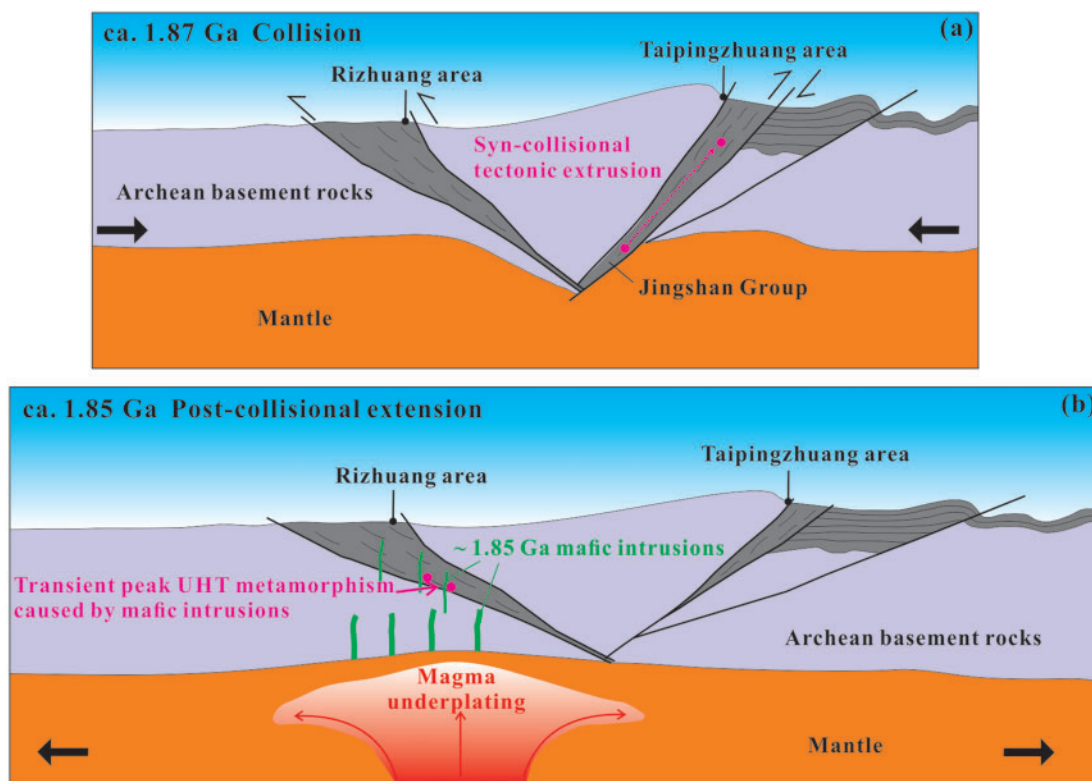
Fig. 16. Schematic illustration showing the inferred tectonic scenarios and associated metamorphic processes in the Taipingzhuang and Rizhuang areas of the Jiaobei terrane. The HPG pelitic granulites in the Taipingzhuang area record a fast decompression-cooling triggered by syn-collisional tectonic extrusion at *c.* 1870 Ma. The pelitic granulites in the Rizhuang area document a transient UHT metamorphism caused by mafic intrusions during post-collisional extension at *c.* 1·85 Ga. (See text for details.)

proterozoic plate tectonics (Brown, 2006, 2007). Global metamorphic archives show that Paleoproterozoic HPG rocks broadly occurred at 2·4–2·5 Ga and 1·8–2·1 Ga (Brown, 2006, 2007; Brown & Johnson, 2018). Extant studies have revealed generally slower cooling (5–30 °C Ma^{-1}) and exhumation of 2·4–2·5 Ga HPG rocks (e.g. Chowdhury & Chakraborty, 2019). Using thermomechanical modeling, Gerya *et al.* (2008) and Chowdhury *et al.* (2017) predicted that slow cooling and exhumation might be characteristics of 2·4–2·5 Ga plate tectonics under hot mantle conditions (hotter by >150 °C compared with present-day mantle; Herzberg *et al.*, 2010). Owing to the hotter ambient mantle, 2·4–2·5 Ga plate tectonics is expected to be different (Holder *et al.*, 2019) because the strength of rocks is strongly temperature-dependent (van Hunen & Moyen, 2012).

Implications for determining ancient metamorphic rates

The ancient fast metamorphic rates defined are compatible with rates estimated by geochronology from their analogs in much younger orogenic belts. For example, the petrography of HPG pelitic granulites from the Taipingzhuang area is comparable with that of the Greater Himalayan Crystalline Complex (e.g. Wang

et al., 2017). The two rock units have similar bulk-rock compositions, almost the same mineral assemblages, and mineral zonation, and thus the same *P–T* path evolution. The much younger Himalayan ages allow precise dating to resolve the rates of fast metamorphic processes. The total duration of decompression and cooling from HPG conditions to ~5 kbar, 600 °C has been constrained to within 3–15 Myr (Daniel *et al.*, 2003; Kali *et al.*, 2010; Grujic *et al.*, 2011; Rubatto *et al.*, 2013; Sorcar *et al.*, 2014; Wang *et al.*, 2017), yielding exhumation and cooling rates that are similar within the same order of magnitude to those from our Paleoproterozoic rocks.

We show that the ancient fast rates determined by garnet geospeedometry do not contradict multi-mineral U–Pb geochronological results (Fig. 15), and that the zircon heavy REE features (Supplementary Data Fig. S11) support the rapid cooling of sample 16SD91. Notably, these ancient fast rates are beyond the temporal resolutions of *in situ* geochronological methods such as SIMS and LA-ICP-MS. The consistent zircon and monazite ages in samples 16SD91 and 16SD117 fail to resolve such ancient fast rates. Moreover, direct employment of monazite/zircon and rutile U–Pb ages will give a single, slower cooling rate. Such a single cooling rate cannot reproduce observed retrograde profiles in garnet

(Fig. 12c and d), and the preservation of multi-stage mineral assemblages probably requires a faster rate at high temperatures. The change in cooling rates also cannot be resolved geochronologically. These observations highlight the limitations of current geochronological approaches in resolving ancient metamorphic rates.

Well-documented examples of short-duration metamorphism are confined to young orogenic belts later than the Neoproterozoic (Rubatto & Hermann, 2001; Pauly *et al.*, 2016; Viete & Lister, 2017), and are exceedingly rare in the early Precambrian (Collins *et al.*, 2004; Baldwin *et al.*, 2007; Guevara *et al.*, 2017; Viete & Lister, 2017). Secular changes in the thermal state and/or chemistry of the crust (Stern, 2005; Gerya *et al.*, 2008; Sizova *et al.*, 2014; Palin & White, 2016; Chowdhury *et al.*, 2017) may have limited short-duration metamorphism (<10 Myr) in ancient times. A likely alternative explanation is that the temporal resolution of geochronology acts as a barrier to resolve rapid metamorphism in old rocks (Viete & Lister, 2017; this study). A conservative uncertainty of 1% in SIMS and LA-ICP-MS U–Pb dating methods means that their temporal resolutions are coarser than 18 Myr when applied to rocks older than 1·8 Ga. Although the $^{207}Pb/^{206}Pb$ age has a better reproducibility, it still fails to resolve an ancient (e.g. *c*. 1·90 Ga) short-duration metamorphic event within 5 Myr, as demonstrated by our case study. Hence, the application of geochronological datasets to the *P–T* paths of early Precambrian orogens could lead to, in most cases, overestimated timescales of specific tectonic–metamorphic processes. The artifactual obscuring of fast metamorphic rates probably more ubiquitous in Precambrian time requires revision of geodynamic models to account for the faster rates of ancient tectonic processes.

CONCLUSION

The Paleoproterozoic pelitic granulites in the Jiaobei terrane display distinct *P–T–t* histories. The pelitic granulites from the Taipingzhuang area record HPG metamorphism (∼12 kbar, ∼800 °C), followed by a fast decompression-cooling to ∼5 kbar and ∼600 °C within 5 Myr. Syn-collisional tectonic-driven exhumation mechanisms at 1870 ± 19 Ma are responsible for the fast decompression-cooling. On the other hand, the studied rocks from the Rizhuang area document a short-lived UHT metamorphism (∼940 °C, <1 Myr), most probably caused by mafic intrusions related to magma underplating during post-collisional extension at *c*. 1·85 Ga.

The juxtaposition and timing of Paleoproterozoic HPG and UHT rocks suggest a sequence of collision and extension. Their fast metamorphic rates are in many ways similar to those for younger metamorphic belts such as the High Himalayan Crystalline Complex. Such modern metamorphic affinities in ancient times coincide with the first global records of high *P*/*T* (<10 °C km^{-1}) metamorphism suggestive of cold subduction, implying that modern plate tectonics may have been operative during the Paleoproterozoic era.

The ancient fast rates defined here with diffusion modeling are beyond the temporal resolutions of *in situ* geochronological methods, which could tend to yield misleading slower rates. Our results thus call for caution when inferring Precambrian tectonic regimes on the basis of apparent, potentially artifactual, protracted metamorphism, and highlight the potential of diffusion geospeedometry as an alternative approach to reveal the rates of ancient metamorphic processes.

SUPPLEMENTARY DATA

Supplementary data are available at *Journal of Petrology* online.

REFERENCES

Ague, J. J. & Baxter, E. F. (2007). Brief thermal pulses during mountain building recorded by Sr diffusion in apatite and multicomponent diffusion in garnet. *Earth and Planetary Science Letters* **261**, 500–516.

Ague, J. J. & Carlson, W. D. (2013). Metamorphism as Garnet Sees It: The Kinetics of Nucleation and Growth. *Elements* **9**, 439–445.

Baldwin, J. A., Powell, R., Williams, M. L. & Goncalves, P. (2007). Formation of eclogite, and reaction during exhumation to mid-crustal levels, Snowbird tectonic zone, western

Canadian Shield. *Journal of Metamorphic Geology* **25**, 953–974.

Bartoli, O. (2017). Phase equilibria modelling of residual migmatites and granulites: An evaluation of the melt-reintegration approach. *Journal of Metamorphic Geology* **35**, 919–942.

Baumgartner, L. (2010). Pressure gradients in garnets induced by diffusion relaxation of major element zoning. In: 2010 GSA Annual Meeting. Denver.

Beaumont, C., Jamieson, R. A., Nguyen, M. H. & Medvedev, S. (2004). Crustal channel flows: 1. Numerical models with applications to the tectonics of the Himalayan–Tibetan orogen. *Journal of Geophysical Research: Solid Earth* **109**, 1–29.

Beaumont, C., Nguyen, M. H., Jamieson, R. A. & Ellis, S. (2006). Crustal Flow Modes in Large Hot Orogens. In: Law, R. D., Searle, M. P. & Godin, L. (eds) *Channel Flow, Ductile Extrusion and Exhumation in Continental Collision Zones. Geological Society Special publication* **268**, 91–145.

Benisek, A., Kroll, H. & Cemic, L. (2004). New developments in two-feldspar thermometry. *American Mineralogist* **89**, 1496–1504.

Bohlen, S. R. & Liotta, J. J. (1986). A Barometer for Garnet Amphibolites and Garnet Granulites. *Journal of Petrology* **27**, 1025–1034.

Borinski, S. A., Hoppe, U., Chakraborty, S., Ganguly, J. & Bhowmik, S. K. (2012). Multicomponent diffusion in garnets I: general theoretical considerations and experimental data for Fe–Mg systems. *Contributions to Mineralogy and Petrology* **164**, 571–586.

Broadwell, K. S., Locatelli, M., Verlaguet, A., Agard, P. & Caddick, M. J. (2019). Transient and periodic brittle deformation of eclogites during intermediate-depth subduction. *Earth and Planetary Science Letters* **521**, 91–102.

Brown, M. (2006). Duality of thermal regimes is the distinctive characteristic of plate tectonics since the Neoarchean. *Geology* **34**, 961–964.

Brown, M. (2007). Metamorphic conditions in orogenic belts: A record of secular change. *International Geology Review* **49**, 193–234.

Brown, M. & Johnson, T. (2018). Secular change in metamorphism and the onset of global plate tectonics. *American Mineralogist* **103**, 181–196.

Caddick, M. J., Konopasek, J. & Thompson, A. B. (2010). Preservation of Garnet Growth Zoning and the Duration of Prograde Metamorphism. *Journal of Petrology* **51**, 2327–2347.

Cai, J., Liu, F. L., Liu, P. H., Wang, F., Meng, E., Wang, W., Yang, H., Ji, L. & Liu, L. S. (2017). Discovery of granulite-facies metamorphic rocks in the Ji'an area, northeastern Jiao-Liao-Ji Belt, North China Craton: Metamorphic P–T evolution and geological implications. *Precambrian Research* **303**, 626–640.

Carlson, W. D. (2006). Rates of Fe, Mg, Mn, and Ca diffusion in garnet. *American Mineralogist* **91**, 1–11.

Chakraborty, S. & Ganguly, J. (1992). Cation Diffusion in Aluminosilicate Garnets—Experimental Determination in Spessartine–Almandine Diffusion Couples, Evaluation of Effective Binary Diffusion Coefficients, and Applications. *Contributions to Mineralogy and Petrology* **111**, 74–86.

Chen, Y., Chen, S., Su, B., Li, Y. B. & Guo, S. (2018). Trace Element Systematics of Granulite-Facies Rutile. *Earth Science* **43**, 127–149.

Cherniak, D. J. (2000). Pb diffusion in rutile. *Contributions to Mineralogy and Petrology* **139**, 198–207.

Chowdhury, P. & Chakraborty, S. (2019). Slow Cooling at Higher Temperatures Recorded within High-*P* Mafic Granulites from the Southern Granulite Terrain, India: Implications for the Presence and Style of Plate Tectonics near the Archean–Proterozoic Boundary. *Journal of Petrology* **60**, 441–486.

Chowdhury, P., Gerya, T. & Chakraborty, S. (2017). Emergence of silicic continents as the lower crust peels off on a hot plate-tectonic Earth. *Nature Geoscience* **10**, 698–703.

Chu, X. & Ague, J. J. (2015). Analysis of experimental data on divalent cation diffusion kinetics in aluminosilicate garnets with application to timescales of peak Barrovian metamorphism, Scotland. *Contributions to Mineralogy and Petrology* **170**, 1–27.

Chu, X., Ague, J. J., Podladchikov, Y. Y. & Tian, M. (2017). Ultrafast eclogite formation via melting-induced overpressure. *Earth and Planetary Science Letters* **479**, 1–17.

Chu, X., Ague, J. J., Tian, M., Baxter, E. F., Rumble, D. & Chamberlain, C. P. (2018). Testing for Rapid Thermal Pulses in the Crust by Modeling Garnet Growth–Diffusion–Resorption Profiles in a UHT Metamorphic 'Hot Spot', New Hampshire, USA. *Journal of Petrology* **59**, 1939–1964.

Clark, C., Fitzsimons, I. C. W., Healy, D. & Harley, S. L. (2011). How Does the Continental Crust Get Really Hot? *Elements* **7**, 235–240.

Clark, C., Kirkland, C. L., Spaggiari, C. V., Oorschot, C., Wingate, M. T. D. & Taylor, R. J. (2014). Proterozoic granulite formation driven by mafic magmatism: An example from the Fraser Range Metamorphics, Western Australia. *Precambrian Research* **240**, 1–21.

Coggon, R. & Holland, T. J. B. (2002). Mixing properties of phengitic micas and revised garnet–phengite thermobarometers. *Journal of Metamorphic Geology* **20**, 683–696.

Collins, A. S., Reddy, S. M., Buchan, C. & Mruma, A. (2004). Temporal constraints on Palaeoproterozoic eclogite formation and exhumation (Usagaran Orogen, Tanzania). *Earth and Planetary Science Letters* **224**, 175–192.

Collins, W. J. (2002). Hot orogens, tectonic switching, and creation of continental crust. *Geology* **30**, 535–538.

Daniel, C. G., Hollister, L. S., Parrish, R. R. & Grujic, D. (2003). Exhumation of the Main Central Thrust from lower crustal depths, Eastern Bhutan Himalaya. *Journal of Metamorphic Geology* **21**, 317–334.

Dong, C. Y., Wang, S. J., Liu, D. Y., Wang, J. G., Xie, H. Q., Wang, W., Song, Z. Y. & Wan, Y. S. (2011). Late Palaeoproterozoic crustal evolution of the North China Craton and formation time of the Jingshan Group: Constraints from SHRIMP U–Pb zircon dating of meta-intermediate–basic intrusive rocks in eastern Shandong Province. *Acta Petrologica Sinica* **27**, 1699–1706 (in Chinese with English abstract).

Droop, G. T. R. (1987). A general equation for estimating Fe^{3+} concentrations in ferromagnesian silicates and oxides from microprobe analyses, using stoichiometric criteria. *Mineralogical Magazine* **51**, 431–435.

Engi, M., Lanari, P. & Kohn, M. J. (2017). Significant Ages—An Introduction to Petrochronology. *Reviews in Mineralogy and Geochemistry* **83**, 1–12.

England, P. C. & Thompson, A. B. (1984). Pressure–Temperature–Time Paths of Regional Metamorphism. 1. Heat Transfer during the Evolution of Regions of Thickened Continental Crust. *Journal of Petrology* **25**, 894–928.

Evans, D. A. D. & Mitchell, R. N. (2011). Assembly and breakup of the core of Paleoproterozoic–Mesoproterozoic supercontinent Nuna. *Geology* **39**, 443–446.

Faryad, S. W. & Chakraborty, S. (2005). Duration of Eo-Alpine metamorphic events obtained from multicomponent

diffusion modeling of garnet: a case study from the Eastern Alps. *Contributions to Mineralogy and Petrology* **150**, 306–318.

Faryad, S. W. & Jezek, J. (2019). Compositional zoning in garnet and its modification by diffusion during pressure and temperature changes in metamorphic rocks; an approach and software. *Lithos* **332–333**, 287–295.

Ferry, J. M. & Spear, F. S. (1978). Experimental calibration of the partitioning of Fe and Mg between biotite and garnet. *Contributions to Mineralogy and Petrology* **66**, 113–117.

Florence, F. P. & Spear, F. S. (1995). Intergranular Diffusion Kinetics of Fe and Mg during Retrograde Metamorphism of a Pelitic Gneiss from the Adirondack Mountains. *Earth and Planetary Science Letters* **134**, 329–340.

Fuhrman, M. L. & Lindsley, D. H. (1988). Ternary-Feldspar Modeling and Thermometry. *American Mineralogist* **73**, 201–215.

Gaidies, F., de Capitani, C. & Abart, R. (2008). THERIA_G: a software program to numerically model prograde garnet growth. *Contributions to Mineralogy and Petrology* **155**, 657–671.

Ganguly, J. (2010). Cation Diffusion Kinetics in Aluminosilicate Garnets and Geological Applications. *Diffusion in Minerals and Melts* **72**, 559–601.

Ganguly, J., Cheng, W. J. & Chakraborty, S. (1998). Cation diffusion in aluminosilicate garnets: experimental determination in pyrope–almandine diffusion couples. *Contributions to Mineralogy and Petrology* **131**, 171–180.

Ganguly, J., Dasgupta, S., Cheng, W. J. & Neogi, S. (2000). Exhumation history of a section of the Sikkim Himalayas, India: records in the metamorphic mineral equilibria and compositional zoning of garnet. *Earth and Planetary Science Letters* **183**, 471–486.

Ganne, J., De Andrade, V., Weinberg, R. F., Vidal, O., Dubacq, B., Kagambega, N., Naba, S., Baratoux, L., Jessell, M. & Allibon, J. (2012). Modern-style plate subduction preserved in the Palaeoproterozoic West African craton. *Nature Geoscience* **5**, 60–65.

Gapais, D., Cagnard, F., Gueydan, F., Barbey, P. & Ballevre, M. (2009). Mountain building and exhumation processes through time: inferences from nature and models. *Terra Nova* **21**, 188–194.

Geisler, T., Schaltegger, U. & Tomaschek, F. (2007). Re-equilibration of zircon in aqueous fluids and melts. *Elements* **3**, 43–50.

Gerya, T. (2014). Precambrian geodynamics: Concepts and models. *Gondwana Research* **25**, 442–463.

Gerya, T. V., Perchuk, L. L. & Burg, J. P. (2008). Transient hot channels: Perpetrating and regurgitating ultrahigh-pressure, high-temperature crust–mantle associations in collision belts. *Lithos* **103**, 236–256.

Glassley, W. E., Korstgard, J. A., Sorensen, K. & Platou, S. W. (2014). A new UHP metamorphic complex in the similar to 1·8 Ga Nagssugtoqidian Orogen of West Greenland. *American Mineralogist* **99**, 1315–1334.

Grujic, D., Warren, C. J. & Wooden, J. L. (2011). Rapid synconvergent exhumation of Miocene-aged lower orogenic crust in the eastern Himalaya. *Lithosphere* **3**, 346–366.

Guevara, V. E. & Caddick, M. J. (2016). Shooting at a moving target: phase equilibria modelling of high-temperature metamorphism. *Journal of Metamorphic Geology* **34**, 209–235.

Guevara, V. E., Caddick, M. J. & Dragovic, B. (2017). Rapid high-*T* decompression recorded by Archean granulites in the northern Wyoming Province: Insights from petrological modelling. *Journal of Metamorphic Geology* **35**, 943–965.

Guo, J. H., Peng, P., Chen, Y., Jiao, S. J. & Windley, B. F. (2012). UHT sapphirine granulite metamorphism at 1·93–1·92 Ga caused by gabbronorite intrusions: Implications for tectonic evolution of the northern margin of the North China Craton. *Precambrian Research* **222**, 124–142.

Harley, S. L. (2016). A matter of time: The importance of the duration of UHT metamorphism. *Journal of Mineralogical and Petrological Sciences* **111**, 50–72.

Harley, S. L., Kelly, N. M. & Moller, A. (2007). Zircon behaviour and the thermal histories of mountain chains. *Elements* **3**, 25–30.

Herzberg, C., Condie, K. & Korenaga, J. (2010). Thermal history of the Earth and its petrological expression. *Earth and Planetary Science Letters* **292**, 79–88.

Hoffman, P. F. (1989). Speculations on Laurentia. *Geology* **17**, 135–138.

Holdaway, M. J. (2000). Application of new experimental and garnet Margules data to the garnet–biotite geothermometer. *American Mineralogist* **85**, 881–892.

Holdaway, M. J. (2001). Recalibration of the GASP geobarometer in light of recent garnet and plagioclase activity models and versions of the garnet–biotite geothermometer. *American Mineralogist* **86**, 1117–1129.

Holder, R. M., Viete, D. R., Brown, M. & Johnson, T. E. (2019). Metamorphism and the evolution of plate tectonics. *Nature* **572**, 378–381.

Holland, T. & Powell, R. (2003). Activity–composition relations for phases in petrological calculations: an asymmetric multicomponent formulation. *Contributions to Mineralogy and Petrology* **145**, 492–501.

HOLLAND, T. & POWELL, R. (1998). An internally consistent thermodynamic data set for phases of petrological interest. Journal of Metamorphic Geology **16**, 309–343.

Holland, T., Baker, J. & Powell, R. (1998). Mixing properties and activity–composition relationships of chlorites in the system $MgO–FeO–Al_2O_3–SiO_2–H_2O$. *European Journal of Mineralogy* **10**, 395–406.

Holness, M. B., Cesare, B. & Sawyer, E. W. (2011). Melted Rocks under the Microscope: Microstructures and Their Interpretation. *Elements* **7**, 247–252.

Ibanez-Mejia, M., Bloch, E. M. & Vervoort, J. D. (2018). Timescales of collisional metamorphism from Sm–Nd, Lu–Hf and U–Pb thermochronology: A case from the Proterozoic Putumayo Orogen of Amazonia. *Geochimica et Cosmochimica Acta* **235**, 103–126.

Indares, A., White, R. W. & Powell, R. (2008). Phase equilibria modelling of kyanite-bearing anatectic paragneisses from the central Grenville Province. *Journal of Metamorphic Geology* **26**, 815–836.

Jamieson, R. A. & Beaumont, C. (2011). Coeval thrusting and extension during lower crustal ductile flow—implications for exhumation of high-grade metamorphic rocks. *Journal of Metamorphic Geology* **29**, 33–51.

Jamieson, R. A., Beaumont, C., Medvedev, S. & Nguyen, M. H. (2004). Crustal channel flows: 2. Numerical models with implications for metamorphism in the Himalayan–Tibetan orogen. *Journal of Geophysical Research: Solid Earth* **109**, 1–24.

Jiao, S. J. & Guo, J. H. (2011). Application of the two-feldspar geothermometer to ultrahigh-temperature (UHT) rocks in the Khondalite belt, North China craton and its implications. *American Mineralogist* **96**, 250–260.

Jiao, S. J., Guo, J. H., Mao, Q. & Zhao, R. F. (2011). Application of Zr-in-rutile thermometry: a case study from ultrahigh-temperature granulites of the Khondalite belt, North China Craton. *Contributions to Mineralogy and Petrology* **162**, 379–393.

Jiao, S. J., Guo, J. H., Wang, L. J. & Peng, P. (2015). Short-lived high-temperature prograde and retrograde metamorphism

in Shaerqin sapphirine-bearing metapelites from the Daqingshan terrane, North China Craton. *Precambrian Research* **269**, 31–57.

Kali, E., Leloup, P. H., Arnaud, N., Maheo, G., Liu, D. Y., Boutonnet, E., Van der Woerd, J., Liu, X. H., Jing, L. Z. & Li, H. B. (2010). Exhumation history of the deepest central Himalayan rocks, Ama Drime range: Key pressure–temperature–deformation–time constraints on orogenic models. *Tectonics* **29**, TC2014, doi:10.1029/2009TC002551.

Kelsey, D. E. & Hand, M. (2015). On ultrahigh temperature crustal metamorphism: Phase equilibria, trace element thermometry, bulk composition, heat sources, timescales and tectonic settings. *Geoscience Frontiers* **6**, 311–356.

Kelsey, D. E. & Powell, R. (2011). Progress in linking accessory mineral growth and breakdown to major mineral evolution in metamorphic rocks: a thermodynamic approach in the $Na_2O–CaO–K_2O–FeO–MgO–Al_2O_3–SiO_2–H_2O–TiO_2–ZrO_2$ system. *Journal of Metamorphic Geology* **29**, 151–166.

Kohn, M. J., Corrie, S. L. & Markley, C. (2015). The fall and rise of metamorphic zircon. *American Mineralogist* **100**, 897–908.

Korhonen, F. J., Brown, M., Clark, C. & Bhattacharya, S. (2013). Osumilite–melt interactions in ultrahigh temperature granulites: phase equilibria modelling and implications for the *P–T*–t evolution of the Eastern Ghats Province. *Journal of Metamorphic Geology* **31**, 881–907.

Kriegsman, L. M. & Alvarez-Valero, A. M. (2010). Melt-producing versus melt-consuming reactions in pelitic xenoliths and migmatites. *Lithos* **116**, 310–320.

Lanari, P. & Duesterhoeft, E. (2019). Modeling Metamorphic Rocks Using Equilibrium Thermodynamics and Internally Consistent Databases: Past Achievements, Problems and Perspectives. *Journal of Petrology* **60**, 19–56.

Lanari, P. & Engi, M. (2017). Local Bulk Composition Effects on Metamorphic Mineral Assemblages. Reviews in Mineralogy and Geochemistry **83**, 55–102.

Lasaga, A. C. (1979). Multicomponent exchange and diffusion in silicates. *Geochimica et Cosmochimica Acta* **43**, 455–469.

Li, Q. L., Li, S. G., Zheng, Y. F., Li, H. M., Massonne, H. J. & Wang, Q. C. (2003). A high precision U–Pb age of metamorphic rutile in coesite-bearing eclogite from the Dabie Mountains in central China: a new constraint on the cooling history. *Chemical Geology* **200**, 255–265.

Li, Q. L., Lin, W., Su, W., Li, X. H., Shi, Y. H., Liu, Y. & Tang, G. Q. (2011a). SIMS U–Pb rutile age of low-temperature eclogites from southwestern Chinese Tianshan, NW China. *Lithos* **122**, 76–86.

Li, S. Z., Zhao, G. C., Santosh, M., Liu, X. & Dai, L. M. (2011b). Palaeoproterozoic tectonothermal evolution and deep crustal processes in the Jiao-Liao-Ji Belt, North China Craton: a review. *Geological Journal* **46**, 525–543.

Li, S. Z., Zhao, G. C., Santosh, M., Liu, X., Dai, L. M., Suo, Y. H., Tam, P. Y., Song, M. C. & Wang, P. C. (2012). Paleoproterozoic structural evolution of the southern segment of the Jiao-Liao-Ji Belt, North China Craton. *Precambrian Research* **200**, 59–73.

Li, X. H., Liu, X. M., Liu, Y. S., Su, L., Sun, W. D., Huang, H. Q. & Yi, K. (2015). Accuracy of LA-ICPMS zircon U–Pb age determination: An inter-laboratory comparison. *Science China Earth Sciences* **58**, 1722–1730.

Li, X. W. & Wei, C. J. (2016). Phase equilibria modelling and zircon age dating of pelitic granulites in Zhaojiayao, from the Jining Group of the Khondalite Belt, North China Craton. *Journal of Metamorphic Geology* **34**, 595–615.

Li, Z. & Chen, B. (2014). Geochronology and geochemistry of the Paleoproterozoic meta-basalts from the Jiao-Liao-Ji Belt, North China Craton: Implications for petrogenesis and tectonic setting. *Precambrian Research* **255**, 653–667.

Liu, F. L., Liu, P. H., Wang, F., Liu, J. H., Meng, E., Cai, J. & Shi, J. R. (2014). U–Pb dating of zircons from granitic leucosomes in migmatites of the Jiaobei Terrane, southwestern Jiao-Liao-Ji Belt, North China Craton: Constraints on the timing and nature of partial melting. *Precambrian Research* **245**, 80–99.

Liu, F. L., Liu, P. H., Wang, F., Liu, C. H. & Cai, J. (2015a). Progresses and overviews of voluminous metasedimentary series within the Paleoproterozoic Jiao-Liao-Ji orogenic/mobile belt, North China Craton. *Acta Petrologica Sinica* **31**, 2816–2846 (in Chinese with English abstract).

Liu, H., Sun, W. D., Zartman, R. & Tang, M. (2019). Continuous plate subduction marked by the rise of alkali magmatism 2·1 billion years ago. *Nature Communications* **10**, 3408.

Liu, J. H., Liu, F. L., Liu, P. H., Wang, F. & Ding, Z. J. (2011a). Polyphase magmatic and metamorphic events from Early Precambrian metamorphic basement in Jiaobei area: Evidences from the zircon U–Pb dating of TTG and granitic gneisses. *Acta Petrologica Sinica* **27**, 943–960 (in Chinese with English abstract).

Liu, J. H., Liu, F. L., Ding, Z. J., Liu, C. H., Yang, H., Liu, P. H., Wang, F. & Meng, E. (2013a). The growth, reworking and metamorphism of early Precambrian crust in the Jiaobei terrane, the North China Craton: Constraints from U–Th–Pb and Lu–Hf isotopic systematics, and REE concentrations of zircon from Archean granitoid gneisses. *Precambrian Research* **224**, 287–303.

Liu, J. H., Liu, F. L., Ding, Z. J., Yang, H., Liu, C. H., Liu, P. H., Xiao, L. L., Zhao, L. & Geng, J. Z. (2013b). U–Pb dating and Hf isotope study of detrital zircons from the Zhifu Group, Jiaobei Terrane, North China Craton: Provenance and implications for Precambrian crustal growth and recycling. *Precambrian Research* **235**, 230–250.

Liu, J. H., Liu, F. L., Ding, Z. J., Liu, P. H. & Wang, F. (2015b). Early Precambrian major magmatic events, and growth and evolution of continental crust in the Jiaobei terrane, North China Craton. *Acta Petrologica Sinica* **31**, 2942–2958 (in Chinese with English abstract).

Liu, P. H., Liu, F. L., Wang, F. & Liu, J. H. (2011b). U–Pb dating of zircons from Al-rich paragneisses of Jingshan Group in Shandong peninsula and its geological significance. *Acta Petrologica et Mineralogica* 30, 829–843 (in Chinese with English abstract).

Liu, P. H., Liu, F. L., Liu, C. H., Wang, F., Liu, J. H., Yang, H., Cai, J. & Shi, J. R. (2013c). Petrogenesis, *P–T*-t path, and tectonic significance of high-pressure mafic granulites from the Jiaobei terrane, North China Craton. *Precambrian Research* **233**, 237–258.

Liu, P. H., Liu, F. L., Wang, F., Liu, C. H., Yang, H., Liu, J. H., Cai, J. & Shi, J. R. (2015c). *P–T*–t paths of the multiple metamorphic events of the Jiaobei terrane in the southeastern segment of the Jiao-Liao-Ji Belt (JLJB), in the North China Craton: Implication for formation and evolution of the JLJB. *Acta Petrologica Sinica* **31**, 2889–2941 (in Chinese with English abstract).

Lu, L. Z., Xu, X. C. & Liu, F. L. (1996). *Early Precambrian Khondalites in North China*. Changchun: Jilin Science and Technology Press, 276 pp. (in Chinese).

Lu, X. P., Wu, F. Y., Gho, J. H. & Yin, C. J. (2005). Paleoproterozoic granitic magmatism and crustal evolution in the Tonghua region, northeast China. *Acta Petrologica Sinica* **21**, 721–736 (in Chinese with English abstract).

Meinhold, G. (2010). Rutile and its applications in earth sciences. *Earth-Science Reviews* **102**, 1–28.

Mezger, K., Hanson, G. N. & Bohlen, S. R. (1989). High-Precision U–Pb Ages of Metamorphic Rutile—Application to the Cooling History of High-Grade Terranes. *Earth and Planetary Science Letters* **96**, 106–118.

O'Brien, P. J. & Rotzler, J. (2003). High-pressure granulites: formation, recovery of peak conditions and implications for tectonics. *Journal of Metamorphic Geology* **21**, 3–20.

Palin, R. M. & White, R. W. (2016). Emergence of blueschists on Earth linked to secular changes in oceanic crust composition. *Nature Geoscience* **9**, 60–65.

Palin, R. M., Weller, O. M., Waters, D. J. & Dyck, B. (2016). Quantifying geological uncertainty in metamorphic phase equilibria modelling; a Monte Carlo assessment and implications for tectonic interpretations. *Geoscience Frontiers* **7**, 591–607.

Pauly, J., Marschall, H. R., Meyer, H. P., Chatterjee, N. & Monteleone, B. (2016). Prolonged Ediacaran–Cambrian Metamorphic History and Short-lived High-pressure Granulite-facies Metamorphism in the HU Sverdrupfjella, Dronning Maud Land (East Antarctica): Evidence for Continental Collision during Gondwana Assembly. *Journal of Petrology* **57**, 185–227.

Peng, P., Wang, X. P., Windley, B. F., Guo, J. H., Zhai, M. G. & Li, Y. (2014). Spatial distribution of ∼1950–1800 Ma metamorphic events in the North China Craton: Implications for tectonic subdivision of the craton. *Lithos* **202–203**, 250–266.

Peressini, G., Quick, J. E., Sinigoi, S., Hofmann, A. W. & Fanning, M. (2007). Duration of a large mafic intrusion and heat transfer in the lower crust: A SHRIMP U–Pb zircon study in the Ivrea–Verbano Zone (Western Alps, Italy). *Journal of Petrology* **48**, 1185–1218.

Powell, R. & Holland, T. J. B. (1988). An internally consistent dataset with uncertainties and correlations. 3. Applications to geobarometry, worked examples and a computer-program. *Journal of Metamorphic Geology* **6**, 173–204.

Pownall, J. M., Hall, R., Armstrong, R. A. & Forster, M. A. (2014). Earth's youngest known ultrahigh-temperature granulites discovered on Seram, eastern Indonesia. *Geology* **42**, 279–282.

Reiners, P. W., Ehlers, T. A., Mitchell, S. G. & Montgomery, D. R. (2003). Coupled spatial variations in precipitation and long-term erosion rates across the Washington Cascades. *Nature* **426**, 645–647.

Rogers, J. J. W. & Santosh, M. (2009). Tectonics and surface effects of the supercontinent Columbia. *Gondwana Research* **15**, 373–380.

Rubatto, D. (2017). Zircon: The Metamorphic Mineral. *Reviews in Mineralogy and Geochemistry* **83**, 261–295.

Rubatto, D. & Hermann, J. (2001). Exhumation as fast as subduction?. *Geology* **29**, 3–6.

Rubatto, D., Chakraborty, S. & Dasgupta, S. (2013). Timescales of crustal melting in the Higher Himalayan Crystallines (Sikkim, Eastern Himalaya) inferred from trace element-constrained monazite and zircon chronology. *Contributions to Mineralogy and Petrology* **165**, 349–372.

Santosh, M., Sajeev, K. & Li, J. H. (2006). Extreme crustal metamorphism during Columbia supercontinent assembly: Evidence from North China Craton. *Gondwana Research* **10**, 256–266.

Santosh, M., Liu, S. J., Tsunogae, T. & Li, J. H. (2012). Paleoproterozoic ultrahigh-temperature granulites in the North China Craton: Implications for tectonic models on extreme crustal metamorphism. *Precambrian Research* **222–223**, 77–106.

Schaltegger, U., Fanning, C. M., Gunther, D., Maurin, J. C., Schulmann, K. & Gebauer, D. (1999). Growth, annealing and recrystallization of zircon and preservation of monazite in high-grade metamorphism: conventional and *in-situ* U–Pb isotope, cathodoluminescence and microchemical evidence. *Contributions to Mineralogy and Petrology* **134**, 186–201.

Schaltegger, U., Schmitt, A. K. & Horstwood, M. S. A. (2015). U–Th–Pb zircon geochronology by ID-TIMS, SIMS, and laser ablation ICP-MS: Recipes, interpretations, and opportunities. *Chemical Geology* **402**, 89–110.

Schulmann, K., Schaltegger, U., Jezek, J., Thompson, A. B. & Edel, J. B. (2002). Rapid burial and exhumation during orogeny: Thickening and synconvergent exhumation of thermally weakened and thinned crust (Variscan orogen in Western Europe). *American Journal of Science* **302**, 856–879.

Sizova, E., Gerya, T. & Brown, M. (2014). Contrasting styles of Phanerozoic and Precambrian continental collision. *Gondwana Research* **25**, 522–545.

Sorcar, N., Hoppe, U., Dasgupta, S. & Chakraborty, S. (2014). High-temperature cooling histories of migmatites from the High Himalayan Crystallines in Sikkim, India: rapid cooling unrelated to exhumation?. *Contributions to Mineralogy and Petrology* **167**, 1–34.

Spear, F. S. (1991). On the Interpretation of Peak Metamorphic Temperatures in Light of Garnet Diffusion during Cooling. *Journal of Metamorphic Geology* **9**, 379–388.

Spear, F. S., Kohn, M. J. & Cheney, J. T. (1999). *P–T* paths from anatectic pelites. *Contributions to Mineralogy and Petrology* **134**, 17–32.

Stern, R. J. (2005). Evidence from ophiolites, blueschists, and ultrahigh-pressure metamorphic terranes that the modern episode of subduction tectonics began in Neoproterozoic time. *Geology* **33**, 557–560.

Tajčmanová, L., Podladchikov, Y., Powell, R., Moulas, E., Vrijmoed, J. C. & Connolly, J. A. D. (2014). Grain-scale pressure variations and chemical equilibrium in high-grade metamorphic rocks. *Journal of Metamorphic Geology* **32**, 195–207.

Tam, P. Y., Zhao, G. C., Sun, M., Li, S. Z., Wu, M. L. & Yin, C. Q. (2012a). Petrology and metamorphic *P–T* path of high-pressure mafic granulites from the Jiaobei massif in the Jiao-Liao-Ji Belt, North China Craton. *Lithos* **155**, 94–109.

Tam, P. Y., Zhao, G. C., Zhou, X. W., Sun, M., Guo, J. H., Li, S. Z., Yin, C. Q., Wu, M. L. & He, Y. H. (2012b). Metamorphic *P–T* path and implications of high-pressure pelitic granulites from the Jiaobei massif in the Jiao-Liao-Ji Belt, North China Craton. *Gondwana Research* **22**, 104–117.

Tang, J., Zheng, Y. F., Wu, Y. B., Gong, B. & Liu, X. M. (2007). Geochronology and geochemistry of metamorphic rocks in the Jiaobei terrane: Constraints on its tectonic affinity in the Sulu orogen. *Precambrian Research* **152**, 48–82.

Thompson, A. B. & England, P. C. (1984). Pressure–Temperature–Time Paths of Regional Metamorphism. 2. Their Inference and Interpretation Using Mineral Assemblages in Metamorphic Rocks. *Journal of Petrology* **25**, 929–955.

Tomkins, H. S., Powell, R. & Ellis, D. J. (2007). The pressure dependence of the zirconium-in-rutile thermometer. *Journal of Metamorphic Geology* **25**, 703–713.

van Hunen, J. & Moyen, J. F. (2012). Archean Subduction: Fact or Fiction? *Annual Review of Earth and Planetary Sciences* **40**, 195–219.

Vavra, G., Gebauer, D., Schmid, R. & Compston, W. (1996). Multiple zircon growth and recrystallization during polyphase Late Carboniferous to Triassic metamorphism in granulites of the Ivrea Zone (Southern Alps): An ion

microprobe (SHRIMP) study. *Contributions to Mineralogy and Petrology* **122**, 337–358.

Vernon, R. H., White, R. W. & Clarke, G. L. (2008). False metamorphic events inferred from misinterpretation of microstructural evidence and *P–T* data. *Journal of Metamorphic Geology* **26**, 437–449.

Viete, D. R. & Lister, G. S. (2017). On the significance of short-duration regional metamorphism. *Journal of the Geological Society, London* **174**, 377–392.

Viete, D. R., Hacker, B. R., Allen, M. B., Seward, G. G. E., Tobin, M. J., Kelley, C. S., Cinque, G. & Duckworth, A. R. (2018). Metamorphic records of multiple seismic cycles during subduction. *Science Advances* **4**, eaaq0234.

Wan, B., Windley, B. F., Xiao, W. J., Feng, J. Y. & Zhang, J. (2015). Paleoproterozoic high-pressure metamorphism in the northern North China Craton and implications for the Nuna supercontinent. *Nature Communications* **6**, 1–10.

Wang, J. M., Zhang, J. J. & Wang, X. X. (2013). Structural kinematics, metamorphic *P–T* profiles and zircon geochronology across the Greater Himalayan Crystalline Complex in south–central Tibet: implication for a revised channel flow. *Journal of Metamorphic Geology* **31**, 607–628.

Wang, J. M., Wu, F. Y., Rubatto, D., Liu, S. R., Zhang, J. J., Liu, X. C. & Yang, L. (2017). Monazite behaviour during isothermal decompression in pelitic granulites: a case study from Dinggye, Tibetan Himalaya. *Contributions to Mineralogy and Petrology* **172**, 1–30.

Waters, D. J. (2001). The significance of prograde and retrograde quartz-bearing intergrowth microstructures in partially melted granulite-facies rocks. *Lithos* **56**, 97–110.

Wei, C. J. (2016). Granulite facies metamorphism and petrogenesis of granite (II): Quantitative modeling of the HT–UHT phase equilibria for metapelites and the petrogenesis of S-type granite. *Acta Petrologica Sinica* **32**, 1625–1643 (in Chinese with English abstract).

Weller, O. M. & St-Onge, M. R. (2017). Record of modern-style plate tectonics in the Palaeoproterozoic Trans-Hudson orogen. *Nature Geoscience* **10**, 305–313.

White, R. W., Powell, R. & Halpin, J. A. (2004). Spatially-focussed melt formation in aluminous metapelites from Broken Hill, Australia. *Journal of Metamorphic Geology* **22**, 825–845.

White, R. W. & Powell, R. (2010). Retrograde melt–residue interaction and the formation of near-anhydrous leucosomes in migmatites. *Journal of Metamorphic Geology* **28**, 579–597.

White, R. W., Powell, R., Holland, T. J. B. & Worley, B. A. (2000). The effect of TiO_2 and Fe_2O_3 on metapelitic assemblages at greenschist and amphibolite facies conditions: mineral equilibria calculations in the system $K_2O–FeO–MgO–Al_2O_3–SiO_2–H_2O–TiO_2–Fe_2O_3$. *Journal of Metamorphic Geology* **18**, 497–511.

White, R. W., Powell, R. & Clarke, G. L. (2002). The interpretation of reaction textures in Fe-rich metapelitic granulites of the Musgrave Block, central Australia: constraints from mineral equilibria calculations in the system $K_2O–FeO–MgO–Al_2O_3–SiO_2–H_2O–TiO_2–Fe_2O_3$. *Journal of Metamorphic Geology* **20**, 41–55.

White, R. W., Powell, R. & Halpin, J. A. (2004). Spatially-focused melt formation in aluminous metapelites from Broken Hill. *Journal of Metamorphic Geology* **22**, 825–845.

White, R. W., Powell, R. & Holland, T. J. B. (2007). Progress relating to calculation of partial melting equilibria for metapelites. *Journal of Metamorphic Geology* **25**, 511–527.

White, R. W., Powell, R., Holland, T. J. B., Johnson, T. E. & Green, E. C. R. (2014). New mineral activity–composition relations for thermodynamic calculations in metapelitic systems. *Journal of Metamorphic Geology* **32**, 261–286.

Whitney, D. L. (1996). Garnet as open systems during regional metamorphism. *Geology* **24**, 147–150.

Whitney, D. L. & Evans, B. W. (2010). Abbreviations for names of rock-forming minerals. *American Mineralogist* **95**, 185–187.

Willigers, B. J. A., van Gool, J. A. M., Wijbrans, J. R., Krogstad, E. J. & Mezger, K. (2002). Posttectonic cooling of the Nagssugtoqidian Orogen and a comparison of contrasting cooling histories in Precambrian and Phanerozoic orogens. *Journal of Geology* **110**, 503–517.

Xu, C., Kynicky, J., Song, W. L., Tao, R. B., Lu, Z., Li, Y. X., Yang, Y. C., Pohanka, M., Galiova, M. V., Zhang, L. F. & Fei, Y. W. (2018a). Cold deep subduction recorded by remnants of a Paleoproterozoic carbonated slab. *Nature Communications* **9**, 8.

Xu, W. & Liu, F. L. (2019). Geochronological and geochemical insights into the tectonic evolution of the Paleoproterozoic Jiao-Liao-Ji Belt. *Earth-Science Reviews* **193**, 162–198.

Xu, W., Liu, F. L., Tian, Z. H., Liu, L. S., Ji, L. & Dong, Y. S. (2018b). Source and petrogenesis of Paleoproterozoic meta-mafic rocks intruding into the North Liaohe Group: Implications for back-arc extension prior to the formation of the Jiao-Liao-Ji Belt, North China Craton. *Precambrian Research* **307**, 66–81.

Yakymchuk, C., Kirkland, C. L. & Clark, C. (2018). Th/U ratios in metamorphic zircon. *Journal of Metamorphic Geology* **36**, 715–737.

Yang, C. & Wei, C. J. (2017). Ultrahigh temperature (UHT) mafic granulites in the East Hebei, North China Craton: Constraints from a comparison between temperatures derived from REE-based thermometers and major element-based thermometers. *Gondwana Research* **46**, 156–169.

Zhai, M. G. & Liu, W. J. (2001). The formation of granulite and its contribution to evolution of the continental crust. *Acta Petrologica Sinica* **17**, 28–38 (in Chinese with English abstract).

Zhai, M. G., Peng, P., Liu, F., Hu, B. & Zhang, H. F. (2009). The metamorphic ages and *P–T* paths of the HT–HP and HT–UHT granulites in North China Craton. *Geochimica et Cosmochimica Acta* **73**, A1502–A1502.

Zhang, B. H., Li, B. W., Zhao, C. C. & Yang, X. Z. (2019). Large effect of water on Fe–Mg interdiffusion in garnet. *Earth and Planetary Science Letters* **505**, 20–29.

Zhao, G. C. & Zhai, M. G. (2013). Lithotectonic elements of Precambrian basement in the North China Craton: Review and tectonic implications. *Gondwana Research* **23**, 1207–1240.

Zhao, G. C., Cawood, P. A., Wilde, S. A. & Lu, L. Z. (2001). High-pressure granulites (retrograded eclogites) from the Hengshan Complex, North China Craton: Petrology and tectonic implications. *Journal of Petrology* **42**, 1141–1170.

Zhao, G. C., Cawood, P. A., Wilde, S. A. & Sun, M. (2002). Review of global 2·1–1·8 Ga orogens: implications for a Pre-Rodinia supercontinent. *Earth-Science Reviews* **59**, 125–162.

Zhao, G. C., Sun, M., Wilde, S. A. & Li, S. Z. (2004). A Paleo-Mesoproterozoic supercontinent: assembly, growth and breakup. *Earth-Science Reviews* **67**, 91–123.

Zhao, L., Li, T. S., Peng, P., Guo, J. H., Wang, W., Wang, H. Z., Santosh, M. & Zhai, M. G. (2015). Anatomy of zircon growth in high pressure granulites: SIMS U–Pb geochronology and Lu–Hf isotopes from the Jiaobei Terrane, eastern North China Craton. *Gondwana Research* **28**, 1373–1390.

Zhong, X., Vrijmoed, J. C. & Tajčmanová, L. (2017). Effect of grain-scale pressure varia-tions on garnet growth: a numerical approach. *Journal of Metamorphic Geology* **35**, 19–33.

Zhou, J. B., Wilde, S. A., Zhao, G. C., Zheng, C. Q., Jin, W., Zhang, X. Z. & Cheng, H. (2008a). SHRIMP U–Pb zircon dating of the Neoproterozoic Penglai Group and Archean gneisses from the Jiaobei Terrane, North China, and their tectonic implications. *Precambrian Research* **160**, 323–340.

Zhou, L. G., Zhai, M. G., Lu, J. S., Zhao, L., Wang, H. Z., Wu, J. L., Liu, B., Zou, Y., Shan, H. X. & Cui, X. H. (2017). Paleoproterozoic metamorphism of high-grade granulite facies rocks in the North China Craton: Study advances, questions and new issues. *Precambrian Research* **303**, 520–547.

Zhou, X. W., Wei, C. J., Geng, Y. S. & Zhang, L. F. (2004). Discovery and implications of the high-pressure pelitic granulite from the Jiaobei massif. *Chinese Science Bulletin* **49**, 1942–1948 (in Chinese with English abstract).

Zhou, X. W., Zhao, G. C., Wei, C. J., Geng, Y. S. & Sun, M. (2008b). EPMA, U–Th–Pb monazite and SHRIMP U–Pb zircon geochronology of high-pressure pelitic granulites in the Jiaobei massif of the North China Craton. *American Journal of Science* **308**, 328–350.

Zou, Y., Zhai, M. G., Santosh, M., Zhou, L. G., Zhao, L., Lu, J. S. & Shan, H. X. (2017). High-pressure pelitic granulites from the Jiao-Liao-Ji Belt, North China Craton: A complete *P–T* path and its tectonic implications. *Journal of Asian Earth Sciences* **134**, 103–121.

Zou, Y., Zhai, M. G., Santosh, M., Zhou, L. G., Zhao, L., Lu, J. S., Liu, B. & Shan, H. X. (2018). Contrasting *P–T*–t paths from a Paleoproterozoic metamorphic orogen: Petrology, phase equilibria, zircon and monazite geochronology of metapelites from the Jiao-Liao-Ji belt, North China Craton. *Precambrian Research* **311**, 74–97.

Zou, Y., Zhai, M. G., Zhou, L. G., Zhao, L., Lu, J. S., Wang, Y. Q. & Shan, H. X. (2019). Relics of a Paleoproterozoic orogen: New petrological, phase equilibria and geochronological studies on high-pressure pelitic granulites from the Pingdu–Laiyang areas, southwest of the Jiaobei terrane, North China Craton. *Precambrian Research* **322**, 136–159.

Zou, Y., Zhai, M. G., Mitchell, R. N., Zhao, L., Zhou, L. G., Liu, B., Wang, Y. Q. & Chen, M. D. (2020). Discovery of kyanite in typically cordierite/sillimanite-bearing low- to medium-pressure pelitic granulites from the Jiaobei terrain. *Precambrian Research* **342**, 105677.